TECHNISCHE UNIVERSITÄT WIEN

DIPLOMARBEIT

An Optimised Catcher-QCM Setup to Study the Sputtering of Lunar and Hermean Surface Regolith Analogues

ausgeführt am Institut für Angewandte Physik
der Technischen Universität Wien
Wiedner Hauptstraße 8-10 / E134
1040 Wien

unter der Anleitung von
Univ.-Prof. Dr. Friedrich Aumayr und
Dipl.-Ing. Herbert Biber, BSc

durch

Johannes Brötzner, BSc
Matrikelnummer: 01605030

[redacted]

Wien, 29. März 2022 Univ.-Prof. Dr. Friedrich Aumayr Johannes Brötzner

Abstract

Rocky bodies in space without a protective atmosphere or magnetic field experience numerous effects. Some of these lead to the liberation of particles from their surface and, subsequently, to the formation of a tenuous so-called *exosphere*. The composition of this exosphere highly depends on the planet's or moon's surface composition and properties and thus provides a possibility for remote surface analysis. Quantitative models on exosphere formation exist, however especially the sputtering contribution is not yet flawlessly described by computational methods. Therefore, this thesis aims to provide experimental data to validate these codes.

Using an advanced Quartz Crystal Microbalance (QCM) setup, the sputtering behaviour of relevant analogue materials is compared between two sample configurations: vitreous films on the one hand and pellets from ground mineral powder on the other. While the thin films are easy to handle and their sputter yields can be studied precisely *in situ* and in real time, the pellets provide a more realistic representation of regolith material, maintaining surface properties like roughness, grain sizes and crystallinity. Two different minerals serve as samples: wollastonite ($CaSiO_3$) and enstatite ($MgSiO_3$). The presented setup was improved during the course of this thesis to allow for automation of major steps of the experiment. Additionally, preparation routines were adapted to allow for reproducible quantification of experimental results.

For irradiations using a 2 keV Ar^+ beam, a main parameter in the description of sputtering of the different sample types is identified as surface roughness. The differences in sputter yield are well modelled using a code based on available Binary Collision Approximation (BCA) simulations, additionally taking the sample surface geometry into account. Sputter yields for the pellet samples are obtained through comparison of the angular distribution of ejecta with the thin film results.

Using 4 keV He^+ ions, on the other hand, the identification of roughness as a single descriptor of the pellet's sputtering behaviour is not as straight forward as for Ar projectiles. A working hypothesis is proposed, according to which roughness effects depend on the size scales of surface features and the typical length scales of ions inside the material. Moreover, roughness effects could be superimposed with crystallinity effects. Further research will be necessary for a clearer untangling of these two contributions. Additional measurements will also give more precise data on pellet sputter yields and lastly, will serve to test the above hypothesis.

Kurzfassung

Gesteinskörper im Weltraum ohne schützende Atmosphäre oder Magnetfeld erfahren eine Vielzahl von Effekten, die zur Freisetzung von Teilchen aus der Oberfläche und in weiterer Folge zur Bildung einer dünnen sogenannten *Exosphäre* führen können. Die Zusammensetzung dieser Exosphäre hängt in hohem Maße von den Eigenschaften der Oberfläche des Planeten oder Mondes ab und bietet somit die Möglichkeit einer Analyse ebenjener. Quantitative Modelle zur Exosphärenbildung existieren, jedoch ist insbesondere der Beitrag der Zerstäubung durch den Sonnenwind noch nicht einwandfrei durch Computersimulationen beschrieben. Diese Arbeit zielt darauf ab, experimentelle Ergebnisse bereitzustellen, um die Simulationsmethoden zu validieren.

Mithilfe eines Quarzkristall-Mikrowaagen-Aufbaus (QCM) wird das Zerstäubungsverhalten relevanter Analogmaterialien zwischen zwei Probentypen verglichen: glasartige Filme einerseits und Pellets aus gemahlenem Mineralpulver andererseits. Während die dünnen Filme einfach handzuhaben sind und ihre Zerstäubungsausbeute präzise *in situ* und in Echtzeit untersucht werden kann, bieten die Pellets ein realistischeres Analog des Regolithmaterials, wobei Oberflächeneigenschaften wie Rauheit, Korngrößen und Kristallinität erhalten bleiben. Zwei verschiedene Minerale dienen als Proben: Wollastonit ($CaSiO_3$) und Enstatit ($MgSiO_3$). Der vorgestellte Aufbau wurde im Laufe dieser Arbeit verbessert, sodass die wichtigsten Schritte des Experiments automatisiert werden konnten.

Für die Bestrahlung mit 2 keV Ar^+ Ionen wurde als Hauptparameter für die Beschreibung des Zerstäubungsverhaltens der verschiedenen Probentypen die Oberflächenrauigkeit identifiziert. Die Unterschiede in der Zerstäubungsausbeute werden mit einem Code gut modelliert, der auf verfügbaren BCA-Simulationen (Binary Collision Approximation) basiert und zusätzlich die Oberflächengeometrie der Proben berücksichtigt. Die Zerstäubungsausbeute für die Pelletproben wird durch den Vergleich der Winkelverteilung der herausgeschlagenen Teilchen mit den Ergebnissen für den Dünnfilm ermittelt.

Bei der Verwendung von 4 keV He^+ Ionen ist die Identifizierung der Rauigkeit als einzig relevanter Parameter für die Beschreibung des Zerstäubungsverhaltens der Pellets nicht ohne weiteres möglich. Es wird eine Hypothese vorgeschlagen, nach der Rauigkeitseffekte von den Größenordnungen der Rauheitsmerkmale und den typischen Längenskalen der Ionen im Festkörper abhängen. Darüber hinaus könnten Rauigkeitseffekte mit Kristallinitätseffekten überlagert sein. Weitere Forschungsarbeit ist erforderlich, um diese beiden Beiträge klarer voneinander zu trennen. Zusätzliche Messungen werden genauere Daten über die Pellet-Zerstäubungsausbeute liefern und schließlich dazu dienen, die obige Hypothese zu testen.

List of Scientific Contributions

Publications in Peer-Reviewed Journals

- N. Jäggi, A. Galli, P. Wurz, H. Biber, P.S. Szabo, **J. Brötzner**, F. Aumayr, P.M.E. Tollan, K. Mezger. *Creation of Lunar and Hermean analogue mineral powder samples for solar wind irradiation experiments and mid-infrared spectra analysis*. Icarus **365**, 114492 (2021)

- C. Cupak, P.S. Szabo, H. Biber, R. Stadlmayr, C. Grave, M. Fellinger, **J. Brötzner**, R.A. Wilhelm, W. Möller, A. Mutzke, M.V. Moro, F. Aumayr. *Sputter yields of rough surfaces: Importance of the mean surface inclination angle from nano- to microscopic rough regimes*. Applied Surface Science **570**, 151204 (2021)

Contributions to International Conferences

- **Poster: J. Brötzner**, H. Biber, P. S. Szabo, N. Jäggi, C. Cupak, A. Nenning, B. Cserveny, A. Galli, P. Wurz, F. Aumayr. *An Optimised Quartz Crystal Microbalance Setup to Investigate Sputtering of Lunar Regolith Analogues*. 34. Symposium on Surface Science 2022 (3S*22), St. Christoph am Arlberg, Austria, 16.3.2022. **Peter Varga Poster Prize 2022**

- **Short Oral Presentation: J. Brötzner**, H. Biber, P. S. Szabo, N. Jäggi, C. Cupak, A. Nenning, B. Cserveny, A. Galli, P. Wurz, F. Aumayr. *An optimised Quartz Crystal Microbalance setup to investigate the sputtering behaviour of bulk targets*. European Geosciences Union General Assembly 2022 (EGU 2022), Vienna, Austria, 23.-27.5.2022 (upcoming).

Supervised Students

Benjamin Cserveny. Bachelor Thesis (ongoing)

Contents

1 Introduction

1.1 Space Weathering and the Solar Wind

In the harsh conditions of space, rocky bodies especially without protective atmospheres experience a variety of influences. These include (micro-) meteoroid impact [1], photon simulated desorption [2] and ion bombardment [3]. Along with their effects of surface erosion and alteration, they are usually summarised under the term *space weathering* [3]. For the Moon, space weathering has an obvious extent: its surface is dotted with craters. Apart from this macroscopic effect, also darkening and reddening of reflectance spectra have been observed [4]. Interaction with ions has been suggested as a mechanism to explain these changes in optical properties [5].

Another consequence of space weathering is the formation of a tenuous so-called *exosphere* [6]. Particles liberated from a planet or moon undergo ballistic trajectories and, depending on their energies, might escape the body's gravitational field. As the composition of the exosphere is tightly interconnected with the underlying surface properties, its analysis provides an opportunity for surface characterisation beyond spectroscopic measurements. This is especially interesting for planets like Mercury, where sample return missions have not yet been performed. In spacecraft flyby missions, the chance arises to investigate an exosphere without the complex and fault-prone task of landing. Such missions have already been carried out, e.g. by the *MESSENGER* spacecraft [7]. The *BepiColombo* mission [8], a collaboration between the European and Japanese space agencies ESA and JAXA, is currently on its way and plans investigations on the interaction between the Sun and Mercury [9]. It has very recently achieved a first gravity assisted flyby of Mercury as a major milestone [10]. So far, the lunar exosphere has been observed to contain the volatile species He, Ar, K and Na [11], while for Mercury H, He, O, Na and K have been detected [12]. As less volatile elements, making up a large fraction of the Hermean mass through rock formation, mainly Ca and Mg have been reported. The erosion of these is argued to be caused mostly due to ion irradiation [12].

On the moon, the main source of ion precipitation is the solar wind. The solar wind is a stream of highly energetic particles originating from the solar corona and ejected through high temperatures and the solar magnetic field [13]. It is generally said to consist of two main constituents: a slow component (≈ 400 km/s) at mid-heliographic latitudes and a fast one (≈ 750 km/s) at high latitudes [14]. In terms of elements, the main species are H and He, which have energies per nucleon in the range of ≈ 1 keV/amu and make up more than 99% of its particle flux [15]. Nonetheless, the influence of heavier minor ions, e.g. C^{4+-6+}, N^{5+-7+}, O^{6+-8+}, Ne^{7+-9+} among oth-

ers [16], on the weathering of airless bodies cannot be neglected. Due to their higher masses, their kinetic sputtering contributions are expected to make up roughly 10% of sputtered particle flux [17]. Additionally, their higher charge states can lead to further enhancement of sputtering due to potential sputtering effects [18].

On Mercury, the situation is slightly different. Although it does not possess a protective atmosphere [19], solar wind ions impact mainly at the poles due to the deflection they experience in the Hermean magnetic field [20]. An additional contribution to ion sputtering on the planet's night side comes from plasma precipitation with origins in Mercury's magnetosphere [21].

Taking all these origins of ion solid interaction, among the other particle release mechanisms, into account, the formation of an exosphere can be simulated. Particularly, this has been done for the Moon [22] and Mercury [6, 23]. However, the underlying data for the sputtering contributions in the above cases were taken from the SRIM simulation code [24] and their validity is questionable. For example, in [25] it has been shown that this code does not reproduce experimental data well and other software like SDTrimSP [26] is a better choice to model these interactions. Nonetheless, also in this better suited code, one might need to adapt parameters like the surface binding energy to achieve agreement with the experiment [18, 27]. Even then, a general shortcoming of the binary collision approximation is the disregard of some properties of real planetary regolith material like roughness or crystallinity. In conclusion, attempts to quantitatively model exosphere formation require experimental data.

This thesis aims to provide such benchmarks for two types of samples from two different minerals. Using the Quartz Crystal Microbalance (QCM) technique, precise sputter yields can be obtained in real time and *in situ* [28]. In an upgrade of the setup, the so-called *catcher configuration* (see section 2.2), also the angular distribution of ejecta can be probed [29]. In this adaptation, a second QCM called *catcher* collects sputtered particle flux from the irradiated samples. Thin amorphous films deposited on quartz resonators represent the mineral stoichiometry well and allow the direct determination of sputter yields [18]. Pellets pressed from ground powder material better represent properties like surface roughness and (poly-) crystallinity, are however more difficult in handling and only give information on the spatial distribution of ejecta. Comparison of the catcher signals between the two sample types can allow to evaluate sputter yields for this type of specimen, too.

1.2 Sputtering Phenomena

The term sputtering denotes the removal of particles from a solid's surface upon bombardment by projectiles with energies ranging from several eV to MeV, thus leading to erosion and henceforth modification of surface morphology and composition [30]. As sputtering depends on many parameters and covers a wide array of physical processes, the following sections shall give a brief overview over the facets relevant for the experiments conducted during this thesis.

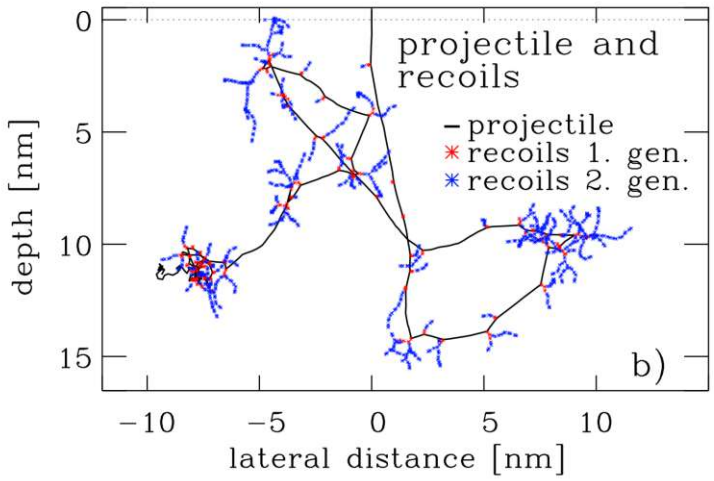

Figure 1.1: Simulation of a collision cascade using the SDTrimSP code. The black solid line traces the trajectory of the projectile, while red and blue represent recoil particles of the first and second generation, respectively. Image taken from [26].

1.2.1 Kinetic and Potential Sputtering

A first extensive explanation of kinetic sputtering was given by Sigmund in [31]. There, the sputtering process is viewed as caused by a series of collisions. An ion entering a solid will at some point collide with a target atom, transferring some of its energy to this very particle. While the recoil is set in motion, the projectile is deflected from its original trajectory and traverses through the solid with less than its original energy. Both collision partners will scatter and lose further energy until they are effectively stopped, forming a so-called collision cascade. An example is depicted in figure 1.1, where the black line symbolises the path of the projectile ion along its way through the solid. Recoils of the first and second generation are shown using red and blue markers, respectively.

In order for a particle to leave the solid, it must acquire sufficient energy to overcome its binding energy to the surface. This necessary energy is associated with a component of momentum perpendicular to the surface, $p_\perp$, via $E = p_\perp^2/(2m)$ where m stands for the particle's mass. This $p_\perp$ is achieved through a series of collisions, every one of which is capable of changing the incident ion momentum vector, such that finally, it is directed outside the surface. It is evident from the need to overcome the surface binding energy (SBE) that sputtering can only occur for projectiles of energies greater than some threshold, usually in the range of some ten electron volts [32]. So far, only the transfer of kinetic energy has been considered. Therefore, it is intuitive that the involved masses of both target and projectile are important to describe the sputtering process as they define how much of the original projectile energy can be transferred in a collision.

Besides these purely kinetic considerations, the ejection of particles from a surface can also be aided by the potential energy of the impinging ion. In this case, one talks about potential sputtering [33], whose principle is briefly described. The term *potential* refers to the energy stored through the removal of electrons from an atom, i.e. it is correlated to a high charge state. As a slow highly charged ion (HCI) approaches the surface, it is further accelerated by its image charge. Before the ion hits the target, resonant neutralisation processes, where electrons are captured in highly excited Rydberg states, lead to partial neutralisation of the ion. The more tightly bound inner states remain empty and a so-called *hollow atom* is formed [34]. Despite the following deexcitation through processes including X-ray and electron emission, some of its potential energy is still available and transferred to the target surface. Here, sputtering is enhanced compared to purely kinetic mechanisms; the origin of this enhancement is currently discussed to be *defect mediated desorption* [35]. Moreover, nanostructuring of the surface is observed [36, 37]. To keep this potential contribution to the sputtering processes as small as possible, all experiments described in this thesis were conducted using singly charged ions.

1.2.2 Sputter Yield

One key quantity to describe sputtering processes is the sputter yield Y. It gives the average information of how many particles are liberated from the target surface normalised per incident ion. It can therefore be defined as

$$Y = \frac{\text{number of sputtered particles}}{\text{number of incoming ions}}. \tag{1.1}$$

Besides the aforementioned dependencies on target and projectile mass as well as the surface binding energy, the sputter yield is also a function of other parameters, most notably the ion beam energy and the incidence angle with respect to the surface normal. The typical dependence of the sputter yield on these two variables is given in figure 1.2. First, the logarithmic plot in figure 1.2a gives the behaviour over the incidence ion energy. The threshold energy is clearly visible. As discussed above, this stems from a need to overcome the surface binding energy. As an incoming ion is most unlikely to transfer its total energy in a single collision to liberate a target surface atom, the sputtering threshold is usually higher than the actual SBE. A maximum of the $Y(E)$ curve is located at about 10 keV. Above this value, the incident ions experience a decrease in the nuclear interaction cross section and therefore stopping power, thus the sputter yield decreases again. Figure 1.2b shows the sputter yield as a function of the ion incidence angle, where 0° means normal incidence and higher angles represent grazing incidence. The plot is normalised to the sputter yield of 0° incidence. A steady increase is observed with increasing incidence angle and a maximum is located at grazing incidences of about 60° to 70° degrees. Two explanations for this behaviour can be given. First, the component of momentum perpendicular to the surface, $p_\perp$, that needs to be transversed, decreases with in-

creasing incidence angle. Therefore, fewer collisions are necessary until ejection of particles is achieved. Additionally, the whole collision cascade becomes skewed under grazing incidence and processes take place in more surface near regions of the target material. For even bigger angles, more ions are reflected and the sputter yield decreases sharply.

1.2.3 Sputtering of Complex Solids

So far, the considerations about sputtering processes were very general. They shall now be expanded to consider features of realistic targets such as surface morphology and composition of more than one element species. The former comes with a range of effects.

First, depending on where the ion hits the surface, it impinges under an angle α_{loc} that is locally different than the global impact angle. As discussed, the sputter yield is a function of the incidence angle with a pronounced behaviour, thus a broad distribution of local surface inclination angles is expected to significantly change the sputtering behaviour compared to a flat surface. The sputter yield at every impact point follows from $Y(\alpha_{\mathrm{loc}})$ rather than depending solely on the nominal incidence angle. Similarly, the impact under a local incidence angle also defines the angular emission characteristic of ejecta. Moreover, ions might get deflected. As they usually maintain sufficient energy, reflected projectiles might cause sputtering a second time, should they hit protrusions on the surface once more. Additionally, also sputtered particles can hit mountains. Due to the low energies with which they are emitted [39], these ejecta do not cause further sputtering and are likely to be redeposited, thus decreasing the net mass flux away from the surface. These effects are shown in figure 1.3, where red and blue arrows denote the ion and particle flux, respectively. The points where ion reflection and ejecta redeposition occur are labelled accordingly. The local incidence angle (here called Θ) is evidently different from the original normal incidence. Finally, there might be areas on the surface that are shadowed from the ion beam such that they never experience ion bombardment.

For composite targets, the different constituent species have different masses and most likely differ in their SBE. Therefore, energy transfer by the same incidence ion beam is unequal between target atom species and one might be more readily sputtered than the other. This effect is called preferential sputtering. In fact, these two reasons (different mass fit, SBE) are attributed to be the main drivers behind preferential sputtering, they can however not solely explain the processes quantitatively [42]. It is noteworthy that with one species more volatile than the other, a fluence dependent change in surface composition takes place. The faster depletion of one constituent leads to enrichment of the less volatile species in the surface region. Eventually, a steady state is reached and sputtering happens according to the original bulk stoichiometry.

As already mentioned, the SBE is an important parameter in the sputtering process, and the lack of knowledge about it is a limiting factor both in the analytic description [31] and the numerical simulation [43]. To complicate things further, the SBE

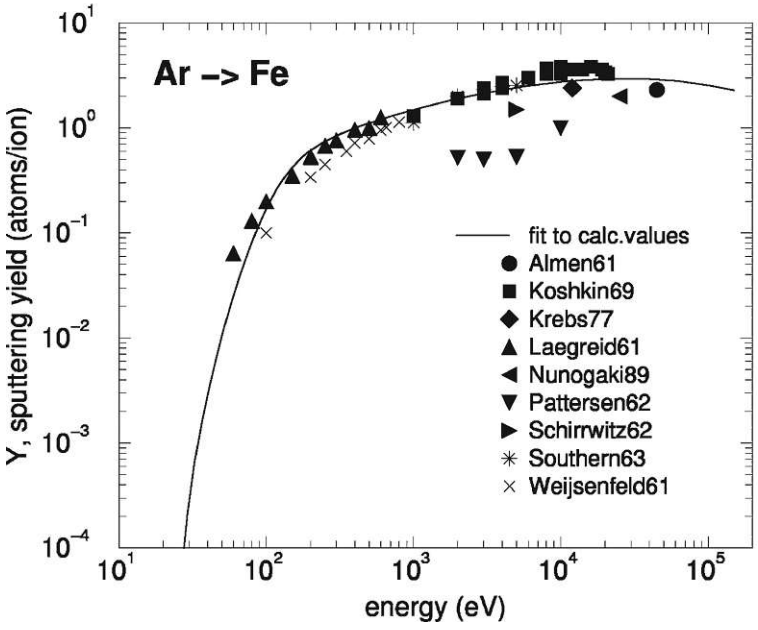

(a)

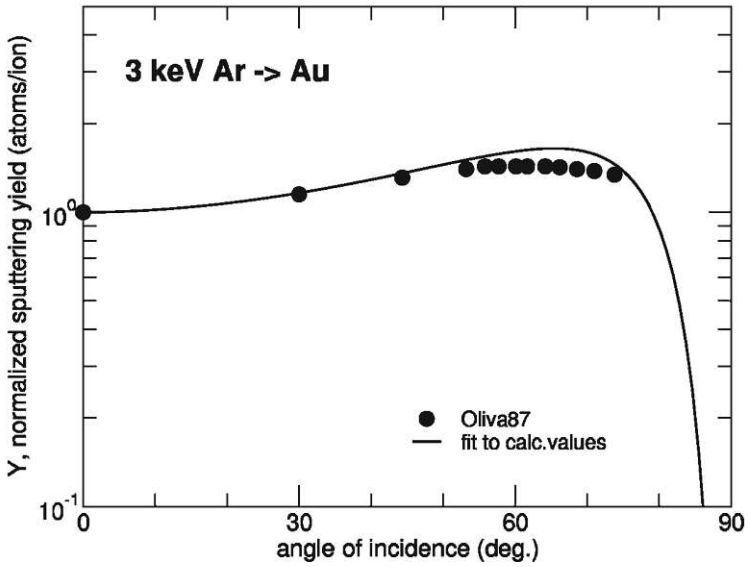

(b)

Figure 1.2: (a): Sputter Yield as a function of incidence ion energy. Visible is the need to overcome a threshold energy for sputtering to occur and a maximum of the sputter yield. At higher energies, the nuclear interaction cross section decreases, and along with it the sputter yield.
(b): Dependence of the sputter yield of the ion incidence angle with respect to the surface normal. A peak is observed for grazing incidence due to more surface near interactions and a small momentum component that has to be flipped. For higher angles still, ion reflection becomes dominant and Y drops. Images taken from [38], the data are cited therein.

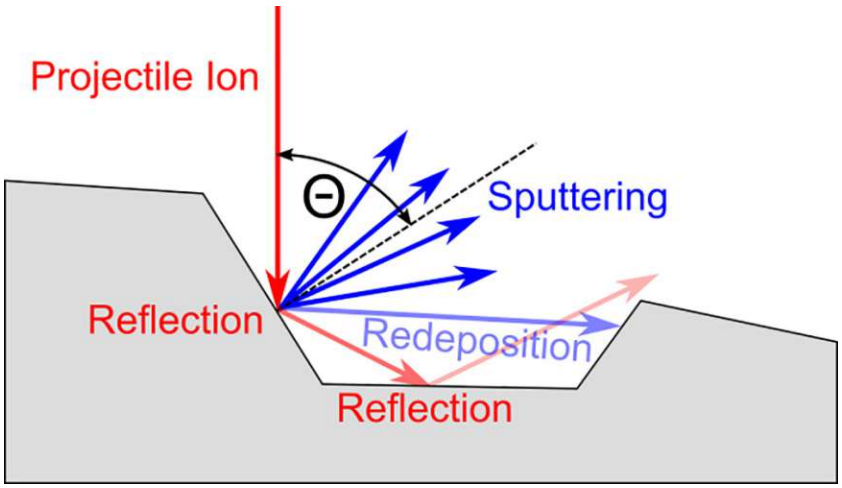

Figure 1.3: Roughness effects on sputtering. Image taken from [40] after [41].

of a given element might not even be the same for mono-elemental and composite samples. It depends on stoichiometry and chemical properties such as coordination to neighbouring atoms and therefore also crystal structure. Often the sublimation enthalpy is used as a first guess [30], however this sometimes does not yield sufficiently precise results. A recent study using molecular dynamics simulations found that for Na, the SBE can vary by up to a factor of ≈ 8, depending on Na concentration in a crystal [44]. In complex minerals, where a single species can have different coordination numbers in building blocks of the unit cell, it might not even be useful to speak of single surface binding energy per element. In fact, current approaches in simulating the sputtering process (see section 1.2.5 below) try to treat silicate minerals as composed of different oxides and assign different SBEs to each. It is hence emphasised that knowledge of the sputtering process is fundamentally limited by the lack of more precise knowledge about surface binding energies.

In single crystalline targets, crystal direction can also play a role. Depending on specific directions and target crystal structure, channels where almost no atoms sit can be formed. If the incident ion beam is directed along such a channel, the ions are scattered almost exclusively with small scattering angles. Thus, their penetration depth might increase and the sputter yield decrease [45]. On the other hand, the presence of many crystal directions has recently been shown to increase the sputter yield compared to amorphous samples due to the presence of linear collision cascades [46].

1.2.4 Energy and Angular Distributions

The yield Y is not the only quantity of interest in the description of the sputtering process. Especially for the experiments with a catching quartz crystal microbalance, knowledge of the energy and angular distributions of ejecta and ions is important for the interpretation of the results.

Figure 1.4 gives the energy distribution of ejected particles showcased for the bombardment of Ca with 4 keV Ar^+ ions under normal incidence. The majority of ejecta are sputtered with energies below 10 eV, which is lower than typical sputter thresholds [32]. They therefore do not cause sputtering on the catcher QCM. As discussed previously, the surface binding energy is a highly unknown parameter. The solid line in figure 1.4 was therefore evaluated using the SBE as a fitting parameter and the obtained value of 1.5 eV is labelled U and given in the legend. An analytic expression for the energy distribution of ejecta was found by Thompson [47]. It predicts a peak at about half of the surface binding energy and a drop off proportional to E^{-2} for energies much higher than the SBE. This behaviour can very well be seen in figure 1.4.

The energy distributions of reflected Ar^+ ions with an original energy of 2 keV impinging on the mineral wollastonite ($CaSiO_3$) is shown in figure 1.5. The orange and blue lines compare incidence under 60° and 80° with respect to the surface normal, respectively. This choice of target and projectile is relevant for experiments in this thesis. The data have been compiled using SDTrimSP simulations (see section 1.2.5). While for the smaller angle most ions are reflected with low energies, there is still a considerable amount above the sputtering threshold. The situation is more extreme for the more oblique angle. Here, the energy distribution peaks just under 2 keV, meaning that a significant amount of ions are reflected with almost no energy loss. This corresponds also to the sharp decrease in the sputter yield seen in figure 1.2b. The drop off before 2 keV is due to the fact that for reflection to take place, at least one collision with a target surface atom has to occur and some amount of energy is always deposited in the target. The ions reflected with energies close to their original energy are also spatially concentrated in the region that corresponds to classical reflection [48]. Therefore, depending on the impact angle on the target, ions can be reflected with energies high enough to cause sputtering at a catcher QCM. The catcher will thus record not only mass accumulation due to sticking of sputtered particles, but the signal will be combined with mass depletion due to sputtering. This effect is expected to be especially prominent with grazing ion impact and at catcher positions that correspond to forward sputtering.

According to [39], under the assumptions of isotropic ion flux under normal incidence and an amorphous target, a $\cos\vartheta$ spatial distribution of ejecta particle flux is expected. Here, ϑ is the angle of emission with respect to the surface normal. This behaviour is not always observed experimentally, however. Due to the highly idealised conditions for which it was derived, deviations occur. Therefore, one often uses a $\cos^y\vartheta$ law to describe the emission characteristic, where y is a fitting parameter, often greater than 1. There are however indications that spatial and energetic distributions are not decoupled and interdepend on each other. Also, under incidence different from 0°, these analytic predictions do not hold anymore. It is therefore desirable to have experimental capacities to probe the angular distribution. One such possibility is given by the catcher QCM configuration described in section 2.2.

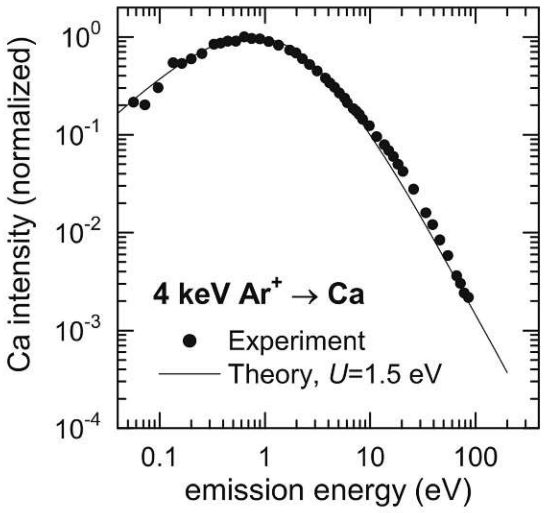

Figure 1.4: Energy distribution of particles ejected by sputtering. Visible is the peak below the SBE (that is also given as a fitting parameter for the theory curve) and the fall off for higher energies. Almost no particles are emitted with energies greater than 10 eV. Taken from [39].

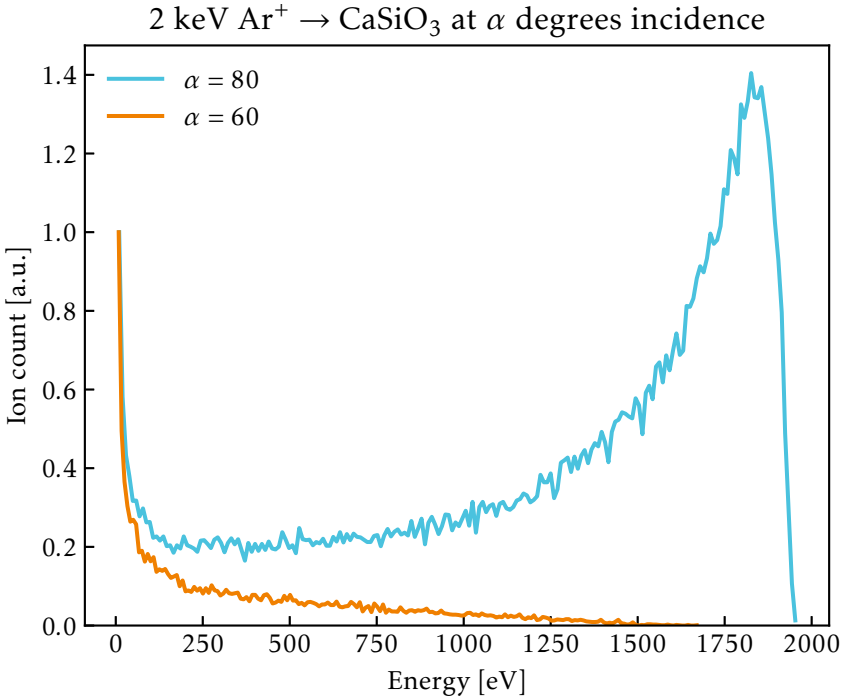

Figure 1.5: Energy distribution of reflected Ar ions after impact on a simulated wollastonite sample for two different incidence angles.

1.2.5 Computer Simulation of Sputtering

For computer simulation of sputtering processes, two main approaches are available. The description below follows the one in [43]. While molecular dynamics (MD) simulations calculate the time evolution of a simulation cell by means of classical equations of motion, binary collision approximation (BCA) codes process individual collisions between two atoms sequentially and independently.

MD simulations can be as accurate as the physical input (i.e. the assumed interaction potentials), they are however limited by a rather small number of simulated particles before they become too computationally expensive. Therefore, BCA codes like the readily available SRIM [24] or SDTrimSP [26] are more widely used. Key assumptions in these are that the collision cascade can be modelled as a series of independent elastic binary collisions. In each of these, the scattering angle is calculated using an effective interaction potential which enters the simulation as an input parameter. Projectile and recoil trajectories are approximated by their asymptotes and particles are tracked until they collide with a different partner. This algorithm is repeated until the particle energy falls under a threshold and it is considered to be stopped. In the special case of Monte Carlo BCA (MC-BCA) codes (as are the two above mentioned), the parameters for each collision (path length between collisions, impact parameter, azimuthal angle) are chosen randomly. Besides the already mentioned interaction potential, other input data are a model for inelastic energy loss between collisions due to electronic stopping, the chosen method of numerical integration and of course the surface binding energy. As discussed above in section 1.2.3, the SBE is amongst the most unknown parameters and can greatly vary for a single element, especially in composite targets or targets where different coordination of this species occurs. This parameter therefore often needs adaptation to achieve agreement with experimental findings, as was done, e.g. in [18] or [27]. Dynamic codes update the target stoichiometry to account for preferential sputtering and ion implantation. For these, a wide range of output information can be gained as a function of ion fluence. This includes, but is not limited to, sputter yields, trajectories of sputtered particles and reflected ions, their respective energy distributions and depth profiles of damages caused by the ion beam.

For the simulation of sputtering of rough realistic surface (in contrast to the flat surfaces of, e.g. SDTrimSP), special versions of simulation codes exist, for example TRI3DYN [49] and SDTrimSP-3D [50]. However, these either require intensive computation infrastructure (recent studies had to be carried out using the Vienna Scientific Cluster), have huge shortcomings in terms of usability or both. As a workaround, a geometric simulation code making use of ray tracing algorithms called *SPRAY* has been developed [29]. It relies on previous studies using conventional MC-BCA codes for a given target-projectile system. Sputter yields, particle trajectories and energy distributions have to be known and provided as input. Using microscopy images of real surfaces (usually by means of atomic force microscopy), a series of random impact point on the surface is chosen. For each one, α_{loc} is calculated and sputtering is assumed to happen according the previously calculated

input data for this angle. Both ejecta and reflected projectile trajectories are chosen using a Monte Carlo approach, and they are traced geometrically until they either reach free space or hit another point on the surface. At this second site of impact, sputtered particles are assume to stick, reducing the net sputter yield. Reflected ions are evaluated according to their energy on whether they can cause secondary sputtering. For a multi-component system, the individual target species are assumed to be independent from another and this process is carried out for each species. The results are then weighted and summed. First results using this approach to describe sputtering of the wollastonite mineral as relevant Hermean regolith analogue were reported in [51].

From the construction of the SPRAY code, its limitations arise naturally: As a lot of input parameters already enter the BCA simulations going into SPRAY, its results can only be as accurate as its input data. Furthermore, SPRAY does not simulate collision cascades at all. Therefore, roughness of the input microscopy images must be on scales where individual mountain flanks can physically be considered flat surfaces for which the input data hold. SPRAY is a purely geometric code, meaning that it does not take into account the length scales on which the ion surface interaction takes place. This could potentially limit the accuracy of results, especially when roughness and the expected size of the collision cascades are of the same order of magnitude. The big advantage of this approach, however, is that there are no limitations in the size of the surface microscopy images. Especially for larger areas, this saves a lot of computation time.

1.3 Outline

This chapter introduced the motivation for and the physical concepts necessary to understand the experiments presented in this thesis. The following chapter 2 will present the main experimental methods, focussing on the quartz crystal microbalance measurement technique, which allows precise determination of sputter yields in real time and *in situ*, and the catcher configuration, that provides a means to probe the angular distribution of sputtered particles. Chapter 3 shall describe the realisation of these techniques in the AUGUSTIN ion beam facility of the Institute of Applied Physics (IAP) at TU Wien. Sample preparation (both creation and cleaning) is described in chapter 4 while experimental findings and their discussion are reported in chapter 5. Finally, chapter 6 provides a summary of the results and a brief outlook to future measurements.

2 Experimental Methods

2.1 Quartz Crystal Microbalance Technique

The Quartz Crystal Microbalance (QCM) technique is a precise method to measure mass changes on a quartz resonator in real time and *in situ* [52]. Over the past years, it has been used extensively at the Institute of Applied Physics (IAP) at the TU Wien [28]. Its working principle is described below.

The QCM is irradiated with an ion beam under an angle of incidence α with respect to the surface normal. This causes the implantation of ions into the sample as well as sputtering of target atoms, both leading to a net mass change. It is possible to resolve this mass change by making use of the quartz's piezoelectric properties: The resonator is coated with two thin Au films that serve as electrodes. An AC voltage is applied to the QCM and a thickness-shearmode oscillation is driven. The corresponding eigenfrequency is tracked using specialised electronics. For small mass changes compared to the initial quartz mass, there exists a linear relation between the resonator mass and its resonance frequency, the Sauerbrey equation [52]:

$$\frac{\Delta m}{m_Q} = -\frac{\Delta f}{f_Q} \tag{2.1}$$

Here, m_Q and f_Q give the original mass and resonance frequency of the QCM, respectively, whereas Δm and Δf denote their changes as a function of time. By introducing the quartz density and its thickness as ρ_Q and d_Q, respectively, it is possible to define a mass change per unit area:

$$\Delta m_A := \frac{\Delta m}{A_Q} = -\frac{\Delta f}{f}\rho_Q d_Q \tag{2.2}$$

Here, A_Q stands for the QCM area. It should be noted that the quartz is not equally sensitive over its whole area. Much rather, its sensitivity decreases radially with increasing distance to the quartz centre and is given by a Gaussian function [52]. In the past, a focussed ion beam has been used at TU Wien to determine the free parameters of the radial sensitivity function [48]. A pair of scanning plates is used to homogeneously irradiate the whole area of non-vanishing sensitivity, which is necessary for equation 2.1 to hold.

According to Sauerbrey, these considerations remain valid also for thin films of a material different than quartz [52]. The above relation 2.2 therefore also holds for a target film under the substitution $\rho_Q \leftrightarrow \rho$ and $d_Q \leftrightarrow d$, where ρ and d denote the

total density and thickness of the whole system (quartz and thin film), respectively. During data evaluation, however, the film thickness and mass can be neglected as they are orders of magnitude smaller than the ones of the quartz alone. Typical film thicknesses are in the range of ≈100 nm whereas the quartz resonators in use have a thickness of about 300 µm.

For experiments in which the target is a compound material, the QCM technique cannot distinguish between the individual contributions of the different target species. Much rather, the absolute mass change per unit area is resolved. To arrive at a mass removal per impinging ion, y, one has to take into account the incidence beam current density j. If it is constant in time and homogeneous over the whole sensitive quartz area, the number of ions N_i hitting the surface during a time Δt is given by

$$N_i = \frac{j \Delta t A_Q}{q e_0}, \tag{2.3}$$

where q is the ion charge state and e_0 denotes the elementary charge. Therefore, one can find an expression for y as follows:

$$y := -\frac{\Delta m}{N_i} = \frac{\Delta f_Q}{f} m \cdot \frac{q e_0}{A_Q j \Delta t} \tag{2.4}$$

The sign is chosen in analogy with the definition of the sputter yield, such that a negative mass change (and therefore positive frequency change) gives a positive mass removal y. Substituting with 2.2 finally yields

$$y = \frac{\Delta f}{f} \rho_Q d_Q \cdot \frac{q e_0}{j \Delta t} = \frac{\Delta f}{\Delta t} \cdot \frac{1}{j} \cdot \frac{\rho_Q d_Q q e_0}{f_Q}. \tag{2.5}$$

Therefore, the expression for y decomposes into a product of three factors: First, $\frac{\Delta f}{\Delta t}$ gives the slope of the frequency over time curve and can be determined from experiments. The second part is merely the incident ion beam current density, which is measured using a Faraday Cup (FC) both before and after each experiment and is therefore known. The final constituent is comprised of constants regarding the QCM itself and is again known.

Due to the high precision, resolution and frequency stability of the setup developed at TU Wien, the QCM technique can be used during sputtering experiments to measure the mass change per incidence ion for mass depletion, whereas commercially available setups are usually used during deposition processes [28]. However, when investigations are carried out using materials as targets that cannot be deposited as thin films onto a quartz resonator, a different approach is used. This upgrade to the QCM setup is described in the following section.

2.2 Catcher-QCM Configuration

As mentioned above, the setup using a single QCM faces restrictions concerning the usable target materials. While it may be suitable for mono-elemental samples, specimens that are comprised of more than a single species might be difficult to reproduce stoichiometrically as a thin film. Additionally, even if the correct composition can be achieved, effects like surface structuring, roughness or crystallinity might be lost or altered during material transfer onto a target QCM. Therefore, a second QCM is placed next to the existing setup, facing the sample to be investigated. If an ion beam hits a target and causes sputtering, particles are liberated. Due to their rather low energies in the range of up to about 50 eV [39], sticking can occur. The purpose of the second QCM is to catch these ejected particles, hence the name *Catcher-QCM (C-QCM)*.

In addition to mass increase on the C-QCM due to the deposition of sputtered target material, other effects have to be considered as well. The incident ion beam might also be reflected from the irradiated sample. Depending on their energy and angle of incidence on the catcher, these reflected ions might sputter material from the C-QCM, leading to a mass decrease. Also, depending on the ion species, and therefore their penetration depth into a given target material, reflected ions might be implanted into the catcher. This would then correspond to a mass increase. Moreover, implanted projectiles might leave the catcher again by outgassing, reducing the resonator's mass. Thus, in a steady state regime, the signal recorded by the C-QCM is a combination of the above mentioned processes. By means of a microbalance alone, their individual contributions cannot be untangled and the resulting frequency over time curve only gives information about the total mass change on the catcher quartz.

In analogy to equation 2.5, a catcher yield y_C can be defined using similar reasonings. It is however important to point out that ejecta contribute to the catcher signal regardless of where on the sample they have been sputtered from. There is no more sensitive area on the irradiated specimen. In contrast to a simple QCM, it is therefore necessary to know the *total* current hitting the target rather than merely the current *density*.

Similarly to equation 2.3, the *total* number ions hitting the target can be defined as

$$N_i^{\text{total}} = \frac{jA_b\Delta t}{qe_0}. \tag{2.6}$$

Here, the sensitive quartz area A_Q has been replaced by A_b, which stands for the total area of the ion beam. It is noted that in the experiment it is ensured that the whole beam hits the target, therefore this area is independent of the ion incidence angle; projection of the ion beam cross section onto the target does not play a role. This is realised by scanning the beam to an area small enough that under no angle of incidence, material other than the sample is hit. Not only is this necessary for the evaluation of the catcher yield to hold, but it also ensures that no material of the target holder is sputtered as this would distort the catcher signal. Similar to the

adaptations to equation 2.3, the mass change per unit area 2.2 is changed to

$$\Delta m = -\frac{\Delta f}{f} \cdot \rho_Q d_Q A_Q \,. \tag{2.7}$$

Equation 2.7 now gives the total mass change of the catcher QCM as a consequence of the Sauerbrey equation. Just as discussed for a simple QCM, A_Q is the area over which the catcher quartz resonator is sensitive to mass changes. In analogy to 2.5, a *catcher yield* y_C can be defined by dividing the expression for the total mass change *on the catcher* 2.7 by the number of ions impinging *on the sample* 2.6, giving

$$y_\mathrm{C} = \frac{\Delta m}{N_i^\mathrm{total}} = \frac{\Delta f}{f} \cdot \rho_Q d_Q A_Q \cdot \frac{q e_0}{j A_b \Delta t} = \frac{\Delta f}{\Delta t} \cdot \frac{1}{I} \cdot A_Q \cdot C \,. \tag{2.8}$$

Of course, this definition still includes and scales linearly with the sensitive area of the catcher quartz. Therefore, a normalisation per solid angle covered by the catcher QCM is introduced and the catcher yield per incoming ion and per steradian is therefore defined as

$$y_{\mathrm{C},\Omega} = \frac{y_\mathrm{C}}{\Omega} = \frac{\Delta f}{\Delta t} \cdot \frac{1}{I} \cdot r^2 \cdot C \,. \tag{2.9}$$

Here, r denotes the distance between the catcher and target centres, respectively. For the herein described experimental setup, the catcher QCM has a sensitive radius of 7 mm outside of which no more mass changes are resolved [48, 53] and $r = 17$ mm. Therefore, the solid angle covered by the catcher is $\Omega \approx 0.13$ sr.

Note that for the case of the C-QCM, a different sign convention has been chosen. Because the mass decrease on an irradiated primary QCM corresponds to a mass increase on the catcher, equation 2.8 does not have a leading minus sign. Instead of the ion current density, the total current I hitting the sample appears.

The experimental realisation of the catcher configuration is sketched in figure 2.1. an ion beam hits a target under an angle of incidence α and causes sputtering of sample material. This angle α can be varied to study the dependence of the sputter yield on the incidence angle. As opposed to preliminary studies using a QCM to collect sputtered particles [54, 55], the current catcher maintains a fixed distance r from its centre to the centre of the irradiated sample. It can be moved in an arc around the target, thereby varying the angle α_C which is defined as the relative angle between the target and catcher surface normals. This geometric variation to previous experiments has an innate advantage: it takes into account the radial symmetry of the experiment. As the flux of sputtered particles through a spherical area with radius r follows an $1/r^2$ law, keeping this r constant allows to meaningfully probe the angular distribution of the ejecta. Before the current setup, only one parameter in a cartesian coordinate system could be varied. Therefore, at every catcher position a different distance to the centre of particle ejection was realised. This changed the recorded signal in addition to the changes expected from a non-isotropic emission characteristic, making the interpretation of results difficult [51, 54].

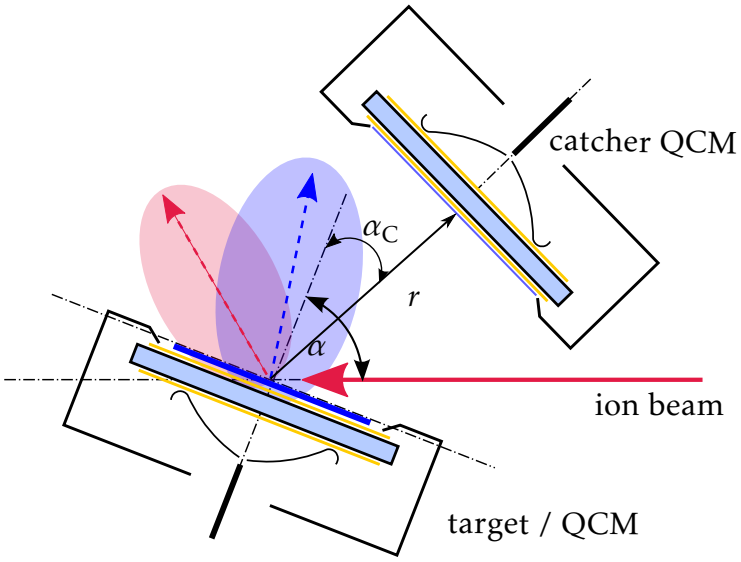

Figure 2.1: A sketch of the catcher setup. A target (depicted is a QCM, it can also be a mineral pellet) is bombarded with an ion beam under an impact angle α. The sputtered particles are collected by a catcher QCM. The angle between the sample and catcher surface normals is given by α_C and the distance between the target and catcher centres is called r. Adapted from [54].

3 Experimental Setup

The experiments described in this thesis were carried out at the *AUGUSTIN* ion beam facility of the Institute of Applied Physics (IAP) at TU Wien. The following section shall trace the path of ions, from their creation in the ion source *SOPHIE* through the Beam Line 3 (BL3) and finally into the experimentation chamber. The layout of the chamber as well as the components of the experiments are described.

3.1 ECR Ion Source "SOPHIE"

The heart of the AUGUSTIN laboratory (spatially, at least) is an Electron Cyclotron Resonance Ion Source (ECR Ion Source or ECRIS, for short) nicknamed SOPHIE (**SO**urce for **P**roduction of **H**ighly charged **I**ons using **E**CR). In such an ion source, a plasma is heated using microwave radiation and confined using magnetic fields in a so-called *minimum-B* field configuration [56, 57]. This is achieved through superposition of an axial magnetic mirror filed and a radial multipole field. In the case of SOPHIE, the multipole field comes from a permanent sextupole magnet. The electrons resonantly absorb the heating radiation in a region where their gyromotion frequency coincides with the microwave frequency. Through collisions with the working gas, atoms thereof are ionised. Additionally, if plasma confinement is good enough, electrons can collide with gas atoms often enough such that subsequent stepwise ionisation to higher charge states is possible.

The microwave signal is produced by an oscillator capable of operation in the range of 6-18 GHz. It is however limited to frequencies of 12.75-14.5 GHz, as this is the acceptable range for the subsequent microwave amplifier. The wave propagates through a rectangular and a cylindrical waveguide, the transition into the vacuum chamber of SOPHIE is provided through a PTFE mirror. To keep reflected power below 20 W (the upper limit the amplifier can withstand), a circulator and an air-cooled dummy load are installed.

Extraction of the ions is realised through an *accel-decel* system consisting of three cylindrically concentric electrodes. This is a system of three electrodes; in addition to the plasma electrode and the extraction electrode held at ground potential, a so-called suppressor electrode is installed between these two. In the plasma extraction region, electrons can be freed either by ionisation of the residual gas or through collisions of the ion beam with the chamber wall metal. These electrons are necessary for space charge compensation in order to reduce ion beam divergence. They are however accelerated towards the plasma and away from the extraction region; therefore, the suppressor is held at a negative potential to repel electrons and thwart them from

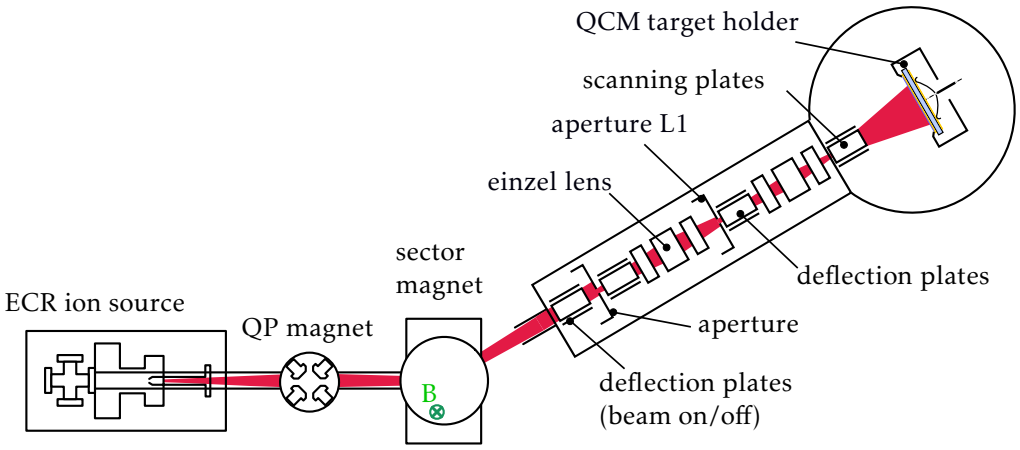

Figure 3.1: A sketch of BL3. Visible are the SOPHIE ECRIS described in section 3.1 along with the subsequent quadrupole magnets and the sector magnet for beam focussing and deflection, respectively. After passing through the bending magnet into the BL3, the ion beam is further shaped using apertures, deflection plates and einzel lenses. The current on aperture L1 can be measured and these data are used to optimally guide the beam into the experimentation chamber. Upon entrance, the ion beam can be scanned to facilitate uniform irradiation over a well-defined sample area. Image adapted from [58].

entering the plasma region. Due to the rather low energies at which the electrons are typically liberated (some ten eV), a potential of -100 V is usually sufficient to achieve this [56]. Ion beam extraction at SOPHIE is possible with acceleration voltages in the range of 1-10 kV, while up to 2 kV can be applied between the suppressor and ground.

3.2 Beam Line 3 (BL3)

Once extracted, the ions are guided through the Beam Line 3 (BL3) of the AUGUSTIN lab. The design of the beam line is briefly described and sketched in figure 3.1. First, the ion beam undergoes focussing in a set of two quadrupole magnets. In such a magnet, two north and two south poles create a magnetic field perpendicular to the ion beam path. Because of the Lorentz force exerted on the ions by this specific B field configuration, focussing is achieved along one plane. In the direction normal to both this plane and the ion beam trajectory, however, the beam is defocussed. To achieve a net focussing effect nonetheless, two quadrupole magnets are placed right after each other, with the second one rotated 90° with respect to the first one.

As a next step, the ion beam passes through a constant vertical magnetic field of a sector magnet. In this field, charged particles are forced to perform circular motion in the horizontal plane around these vertical field lines. The radius of curvature

for these trajectories depends on the ions' charge state and mass, their acceleration voltage and the B field itself. Using a simple balance of forces in which the centripetal force is given by the Lorentz force, this radius can be expressed as a function of the ion velocity. By means of an energy balance, the velocity is found to depend only on the ions charge state, mass and acceleration voltage. The above findings considered, a relation can be established in which the mass over charge ratio, m/q, is linearly dependent on the squared magnetic field. Thus, by varying the B field, a mass over charge selection takes place. This is used to deflect ions of a desired m/q ratio into the correct beam line. Moreover, unwanted charge states or ion species (e.g. from contaminations, residual or mixing gases inside the SOPHIE vacuum chamber) are separated from the beam with which experiments are carried out. In fact, in [59] a brief analysis of this $m/q \propto B^2$ behaviour was carried out using data from the previous years of experiments and excellent agreement to this simple relation was found.

After deflection into BL3 by the sector magnet, the ion beam current can be measured by means of a Faraday Cup that is pneumatically movable into and out of the beam path. It is used to pre-adjust the beam and for taking mass over charge spectra. A pair of deflection plates is mounted at this position in order to allow for electronic switching between "beam on" and "beam off". Afterwards, the beam passes two sets of ion beam optics, each one consisting of one aperture, two pairs of deflection plates and one einzel lens. While the apertures are used to shape the ion beam based on purely geometric effects, both the deflection plates and the einzel lenses work by exerting a Lorentz force on the ions. In a pair of deflection plates, a constant voltage is applied to the two parallel plates such that a homogeneous electric field arises. The ions undergo parabolic trajectories in this field, which results in a deflection of the ion beam. Using a pair of such plates, the beam can be steered in the plane perpendicular to its original velocity vector. An einzel lens is a set of three concentric cylinders in which a voltage is applied to the middle one while the other two are held at ground potential. Due to the radial potential gradient, ions travelling closer to the cylindrical centre axis experience a different force than the ones farther off-centre and a net focussing effect is achieved. In the BL3 setup, one of the apertures (labelled *L1* in figure 3.1) is connected to a picoammeter. It is used in navigating the ion beam into the experimentation chamber. While no beam optics devices are active, an operating point of the quadrupole magnets is found to maximise current on this L1 aperture. Subsequently, the first set of deflection plates and the first lens are used such that the now focussed beam passes through L1. The second set of beam optics is then utilised to maximise ion current in a Faraday Cup inside the experimentation chamber. At the very entrance to this chamber, the focussed beam is scanned over the target by means of a pair of scanning plates. Sawtooth voltages of 1.6 kHz and 52 Hz are applied to the two pairs, respectively, to ensure homogeneous irradiation over a well-defined sample area [53].

3.3 Experimentation Chamber

The central part of the experimentation chamber is the sample holder, which is shown in figure 3.2. It is mounted to a manipulator that can be moved along three planes of motion and rotated around its centre axis. All of these degrees of freedom can be accessed by means of stepper motors such that automation of measurements is possible. Consisting of three compartments, the following objects are mounted to the sample holder:

1. Faraday Cup (FC): A Faraday Cup is used for current measurements of the ion beam. A suppressor held at -56 V is used to repel electrons that are liberated from the FC wall through ion impact so as not to alter the current measurement. Through the motorisation of the manipulator, the FC can be moved along a cross in the plane perpendicular to the ion beam. This is used to gauge the geometry of the ion beam and to determine the total ion current impinging on the samples.

2. QCM: A quartz crystal microbalance with a thin film of a sample material deposited onto it. This QCM is used to investigate yields of these thin films through direct irradiation. Additionally, it is also bombarded during catcher measurements to compare the angular distribution of ejecta between amorphous films and pressed pellets. Moreover, as primary data is directly accessible through this QCM, it can be used to check whether any unexpected disturbances caused the ion beam current density to change over the course of the irradiation. Such data is not available from exclusive pellet irradiations.

3. A pellet pressed from material representative for the surface of Mercury. With its polycrystalline structure it resembles a more realistic analogue than amorphous thin films and can be used to find possible differences between both systems upon ion beam irradiation.

The QCM and the pellet are both equipped with a K type thermocouple and heating wires. These are relevant for multiple use cases. From a scientific viewpoint, measuring temperature dependent effects might be interesting and has already been carried out with this setup [60]. On a purely technical side, heating the samples can be required during preparation (see, e.g. section 4.4), or a controller can be used to operate the QCM at a working point where its eigenfrequency as a function of temperature is minimal [28].

Flanged onto the experimentation chamber from underneath is another $xyz\varphi$ manipulator. It is, however, only equipped with a single stepper motor responsible for automation of the rotation around its centre axis. The manipulator houses the holder for the catcher QCM and, as an extension of the central rod, a mandrel. The sleeve counter piece is mounted to the bottom of the primary sample holder such that the mandrel can be inserted into the sleeve. When connected, this construction limits the possible motion of both manipulators to vertical translation and rotation along

their centre axes. This ensures a constant distance between the midpoint of the irradiated sample and the centre of the catcher QCM. Therefore, the same geometry between measurement cycles is assured while the ability to vary the catcher angle α_C is maintained. To facilitate smooth motion between the two components, they are lubricated using MoS_2 powder which retains its lubricating properties also in vacuum [61]. Contrary to the pellet and primary QCM, neither thermocouple nor heating wires are currently installed with the catcher holder. While a holder with a heating facility exists, it was redesigned and rebuilt during the time span of this thesis. By removing the heating wires, space was gained to slim down the holder. Due to an asymmetric design and a frame as thin as possible to safely hold the quartz, a smaller minimal angle with respect to the incoming ion beam is achieved before shadowing the scanned beam. Therefore, a larger solid angle can be probed. The original holder is still available and can be installed with little effort, should heating of the catcher become a requirement. The technical drawings for the adapted holder are given in the appendix. A CAD render of the both sample and catcher holder illustrating the sleeve and mandrel guiding mechanism is given in figure 3.2. Shown is still the symmetric catcher holder design with heating wires.

While irradiation of a thin film on a QCM with an ion beam does not pose a problem as far as charging up of the sample is concerned (as was demonstrated in [62]), this is very well the case for thick insulating pellets. Therefore, an electron flood gun is installed to provide low energy electrons which counteract the accumulation of positive charge on the sample due to the impinging ions. This could lead to deflection of the beam such that sputtering of the sample holder might occur, thus altering the catcher signal and contaminating the pellet with foreign material. Moreover, making use of the effect of electron stimulated desorption, the flood gun is also used when samples are to be cleaned without the possibility of sputtering. Communication with the flood gun controller is carried out via the Modbus TCP protocol as implemented by the `pyModbusTCP` library [63]. A program was developed to enable remote controlling of the flood gun. In addition to switching the operation on or off, the operation parameters can be set and are periodically saved to a log file. In case the gun fails, a reset is attempted and a pre-defined experimenter is notified via e-mail.

A similar attempt in measurement remote control and automation was made by developing by a graphical user interface (GUI) with which all the beam optics devices discussed in section 3.2 can be controlled. It acts as a central panel from which the beam can be shaped and the relevant current measurements (L1 aperture, see figure 3.1, and the FC on the sample holder) are plotted in real time. Additionally, the ion beam shape can be investigated using pre-defined programs to measure beam profiles. All settings can be saved and loaded such that easy recreation of previous mesaurement conditions is achieved. The details of implementation and a user manual can be found in [64].

The vacuum chamber is pumped by two ion getter pumps and, if necessary, a turbomolecular pump. Base pressures are typically in the medium to high 10^{-10} mbar range and therefore, ultra-high vacuum (UHV) conditions are achieved. If desired, a titanium sublimation pump can also be fired to aid the other pumps.

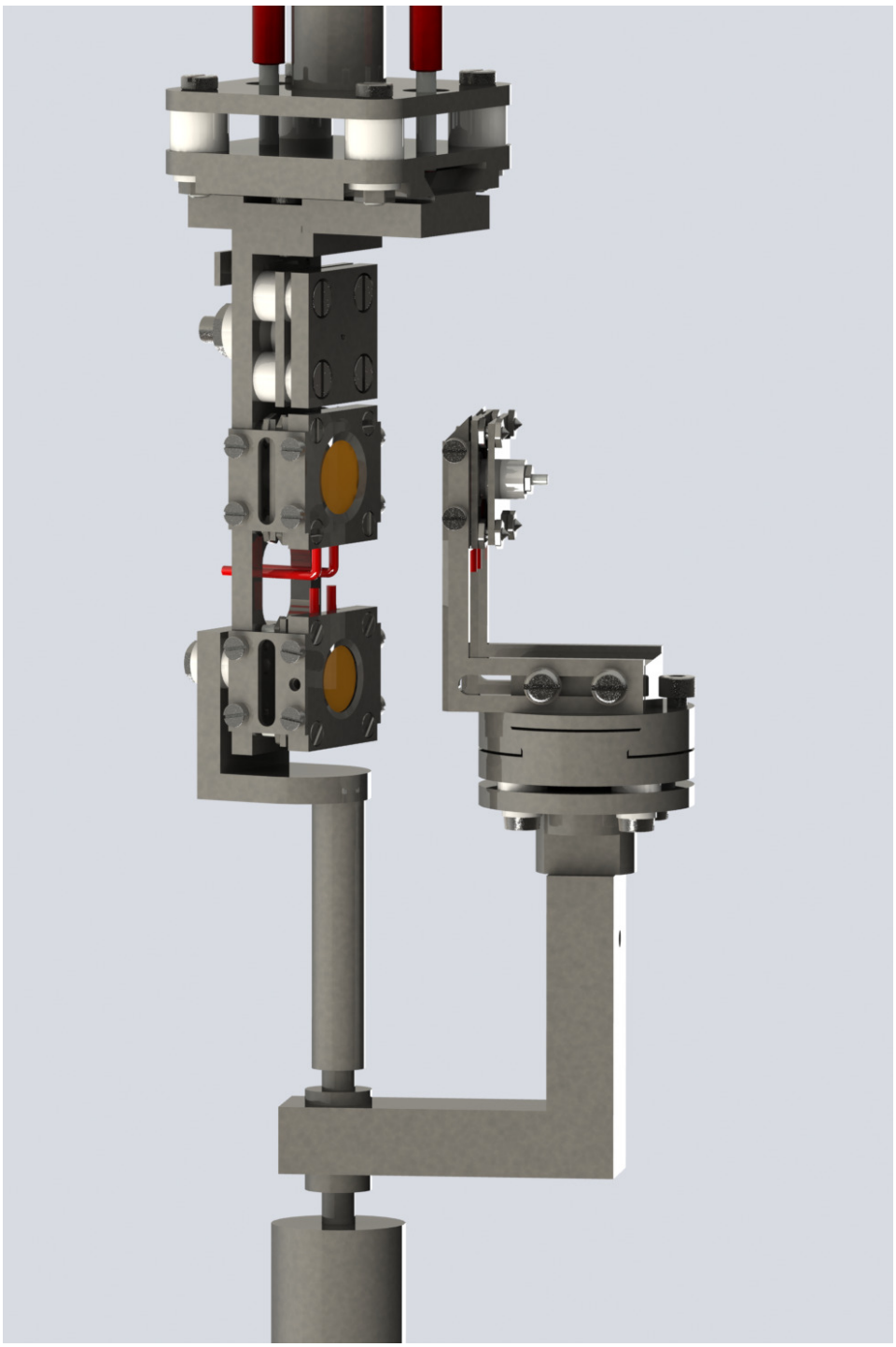

Figure 3.2: A render of the sample holder and catcher QCM in the vacuum chamber. The manipulators can be connected to each other via insertion of a mandrel into a (MoS_2 lubricated) sleeve, fixing the experimentation geometry. When inserted, only rotation remains as a degree of freedom for both manipulators. The sample holder houses three compartments, from top to bottom: a Faraday Cup, a QCM with a deposited sample film and a mineral pellet.

3.3.1 QCM Electronics and Controlling

As discussed in section 2.1, sputter yield information in a QCM setup is gained through precise tracking of the quartz resonance frequency. For this purpose, two possibilities are available at the BL3 experiment, both of which rely on a feedback voltage generated by a so-called phasebox. It is mounted outside the vacuum chamber and connected to the quartz via a feedthrough. A sine wave voltage is fed into the phasebox while a voltage controlled amplifier is used to maintain a constant current through the quartz. The phasebox output signal now depends on the difference between the input frequency and the quartz' series resonance frequency and is established through a phase comparison between current and voltage. If in resonance, this phase shift is zero and leads a zero voltage output. Otherwise, the output is a non-vanishing DC voltage and controllers lock onto this zero crossing of the output. By means of a differential setup and a dummy cable of the same length as the actual QCM signal cable, its capacitance is compensated for. The precise electronics are described in [65] while repair and suitable replacement parts are discussed in [62].

To record the QCM resonance frequency, a setup using a function generator equipped with an oven-controlled crystal oscillator reference frequency can be used. The phasebox output is fed into a personal computer (PC) by means of a fast analog-digital-converter (ADC). A proportional-integral-derivative (PID) controller written in the Python programming language [66] is then used to derive the needed function generator output. This setup (as described in [67]) has the advantages that it does not require a frequency counter and that overtone oscillations can be excited quasi simultaneously. However, using the setting of [67], a single data point is recorded only every five seconds. Moreover, noise was usually in the range of about 10 mHz. This combination of a bad time resolution and a rather noisy signal is not ideal for the catcher configuration, where signals are inherently much smaller compared to frequency curves of quartzes that are directly irradiated. That is why this means of controlling is used to record the eigenfrequency of the primary sample QCM.

On the other hand, a well-tried approach as described in [28] and [65] is applied to measure the catcher resonance frequency. A low noise LC oscillator is used. Its frequency is tunable between 59 and 61 MHz and is fed both into a frequency counter and a Johnson counter. While the former is used to log the frequency, the latter divides the signal by 10 for driving the QCM series resonance. In previous implementations of this approach, the frequency counter was controlled using a LabView [68] program, taking one data point every second with a measurement time of 10 ms. LabView is commercial software and requires internet connection to communicate with a licensing server upon startup. However, due to security concerns, the PC was taken off the internet and therefore, a different solution had to be established. Preliminary attempts with this transition from proprietary software to home-made tools based on the freely available programming language Python had failed due to poor and simplistic construction of these first command line based tools. Again, a graphical user interface was developed. Its function follows an event based paradigm allowing to circumvent the limitations of the initial controlling attempts. The most

notable of these shortcomings was that no proper termination of device communication was carried out, leaving the frequency counter in a state unable to accept new data reading prompts. The resulting software also provides experimental benefits: A measurement time of one second is set at the frequency counter, and a new data point is recorded as soon as the last one is processed, giving again a sample rate of roughly one data point per second. This is an improvement of a factor of 5 compared to the above described setup using a function generator, and due to the prolonged integration time also compared to the LabView version. Now, signals usually carry noise in the 2-3 mHz range in contrast to the 10 mHz described above. This low noise is especially important for naturally small signals on the catcher QCM and the better time resolution is imperative for experiments where only low fluence can be applied to specimens. The new controlling software is described in detail in [64].

4 Sample Preparation and Data Evaluation

4.1 Choice of Analogue Materials

The surfaces of celestial bodies is covered by so-called regolith, a loose layer of fractured bedrock, whole rocks and single crystal agglutinates [69]. While composition of lunar regolith can be analysed through material brought back to earth from sample return missions, the Hermean mineralogy can be estimated by means of remote sensing. In both cases, pyroxene and plagioclase minerals seem to appear on the respective surfaces [70, 71]. As a member of the pyroxene family, the mineral enstatite ($MgSiO_3$) has been chosen. Additionally, experiments were carried out with samples of the pyroxenoid wollastonite ($CaSiO_3$). Even though not directly an analogue material for neither the Moon nor Mercury, it is ideally free of Fe and thus serves to represent Hermean silicates with low iron content [72].

4.2 Creation of Thin Films

The thin films investigated during this thesis were deposited onto quartz resonators by means of Pulsed Laser Deposition (PLD). PLD is considered to be a suitable technique for the stoichiometric formation of films from composite materials [73]. In this method, energy in the form of laser pulses is deposited in a sample, leading to the ablation of material and a plasma plume above the irradiated sample. This plume hits a substrate, e.g. a QCM, and a thin film is formed. The samples for the presented experiments were prepared by A. Nenning of the Institute of Chemical Technologies and Analytics at TU Wien.

The wollastonite films were prepared using a 248 nm KrF excimer laser. Typical PLD parameters were 5-10 Hz pulse frequency and a fluence of 1-3 Jcm^{-2} per pulse under an atmosphere of 4×10^{-2} mbar O_2. The sample was heated to 270 °C and the depositions were carried out for a time span between 30 and 60 minutes. The resulting films were analysed for thickness and composition using ion beam analytics at Uppsala University. Donor material was a wollastonite crystal provided by the University of Bern. Rutherford Backscattering Spectrometry found thicknesses varying between 30 nm and 700 nm, depending on PLD parameters. Time of Flight - Elastic Recoil Detection Analysis (ToF-ERDA) and X-ray Photoelectron Spectroscopy found stoichiometry of the original wollastonite material to be well reproduced, despite some C contaminations that resulted from transportation of the samples on air [18].

The same PLD setup was used for the deposition of enstatite films. However, the focus spot size of the laser was reduced, resulting in a fluence of about 3 Jcm^{-2} per pulse. This was done in order to achieve a more even film growth with less mesoscopic particles on the QCM. Deposition times ranged between 15 and 30 minutes. All other parameters were kept the same as for the wollastonite samples. In contrast to the above described wollastonite, no suitable single piece of enstatite mineral was available for the use in PLD. Therefore, deposition was carried out using a pressed enstatite pellet as donor (see section 4.3 below).

Figure 4.1 gives an overview of the resulting films. Figures 4.1a and 4.1b show Atomic Force Microscopy (AFM) images of the wollastonite and enstatite films, respectively. Visible are also some mesoscopic chunks that appear on the samples due to the PLD process. The formation of these bigger particles has also been reported by other investigators [74]. Nonetheless, past investigations in the Atomic and Plasma Physics (APP) group concluded using X-ray Diffraction and ToF-ERDA that besides these chunks, also a coherent and amorphous sample film covering the Au electrode on the quartz is formed [18, 48]. Given in figure 4.1c is a photo of one resulting sample, in this particular case of a $CaSiO_3$ film. It is thin and translucent enough that the underlying electrode can be seen. Finally, figure 4.1 shows an analysis of the Surface Inclination Angle Distribution (SIAD) for both sample films. This distribution gives information on how much local surface normals deviate from the global surface normal. Its mean value has recently been observed to be an important predictor on how much sputter yields change for a rough surface compared to a perfectly flat one [29]. The plotted distributions have been normalised with respect to their maximum value. For both sample minerals, the SIADs peak at about 10° and most inclination angles are below 20°. It is therefore concluded that both $CaSiO_3$ and $MgSiO_3$ give comparably smooth films using PLD sample preparation.

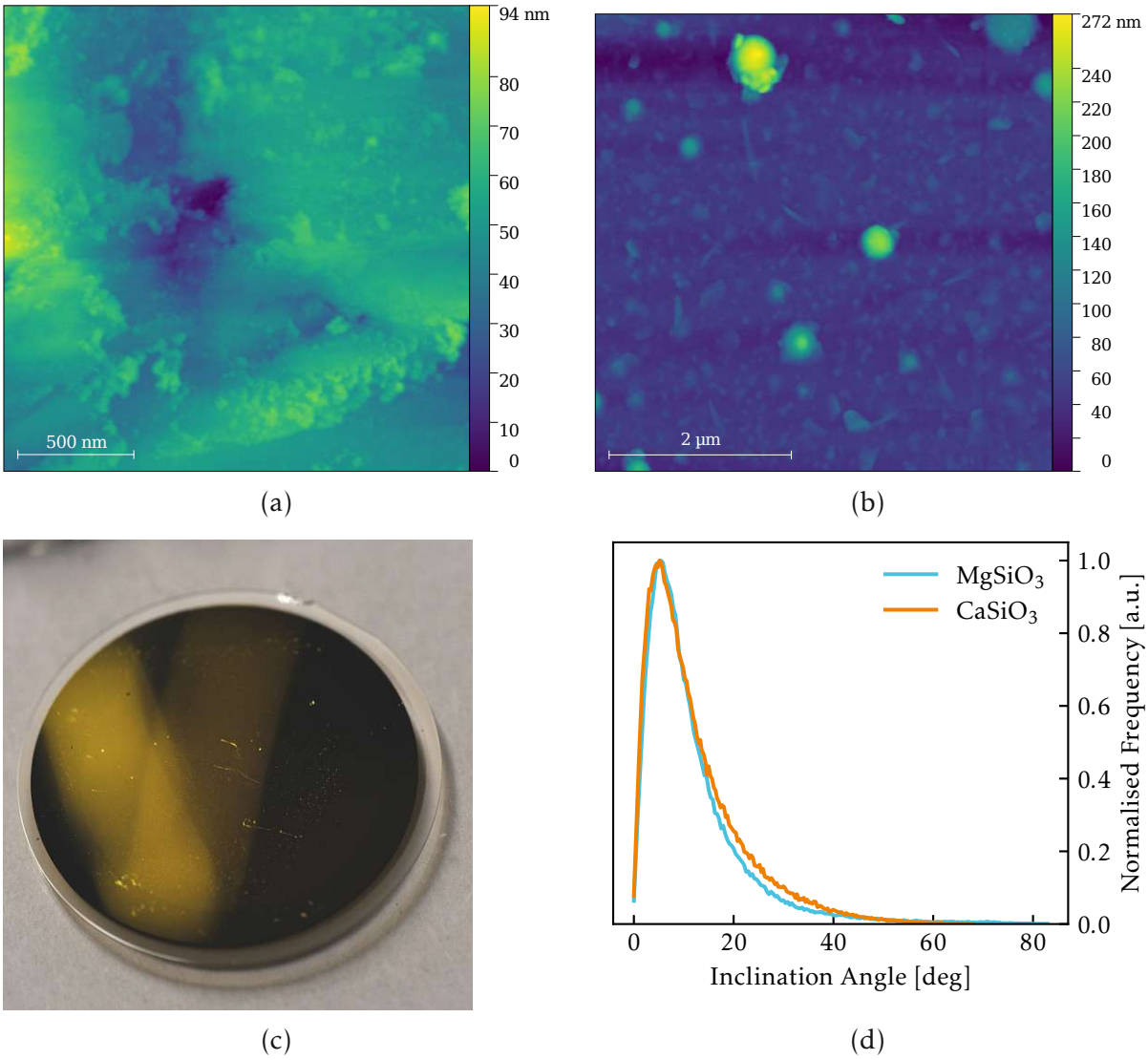

Figure 4.1: (a): AFM image of a wollastonite film.
(b): AFM of image of an enstatite film.
(c): photo of a wollastonite film deposited on a QCM.
(d): SIAD of mineral films of the both investigated sample minerals

	Wollastonite	Enstatite
SiO_2	52.22 ± 2.37	55.47 ± 3.91
Al_2O_3	b.d.	0.70 ± 0.50
FeO	b.d.	5.22 ± 0.65
MgO	b.d.	38.61 ± 3.25
CaO	47.78 ± 1.37	b.d.

Table 4.1: Composition of minerals used in pellet pressing. All values in wt%, oxide contents below detection limits are labelled as "b.d.". Data taken from [69].

4.3 Creation of Mineral Pellets

As a second type of sample, pressed mineral pellets were prepared at the University of Bern. The preparation process is described in [69] and briefly sketched. Wollastonite and enstatite were ground in an agate disk mill. The resulting powder was investigated for grain size and subsequently filtered. In a first attempt, about 0.3 g of the mortared material were pressed between two pistons by applying 239 MPa of pressure for 5 minutes. The result was then glued onto a stainless steel holder by means of a UHV and high temperature safe carbon-based paste. This approach was sufficient to produce a mechanically stable pellet of wollastonite. For enstatite however, the resulting sample was delicate and broke easily. To counteract this problem, a reduced amount of material (≈ 0.03 g) was pressed directly into the steel holder. To improve cohesion, a base of wollastonite was first produced upon which the enstatite was pressed.

Again, chemical composition was analysed, this time using scanning electron microscopy. The relevant results are given in table 4.1. It is apparent that the wollastonite base material did in fact not contain Fe, as was desired. Thus it can act as an ideal Ca-silicate pyroxenoid to simulate Hermean regolith, even though it is not expected to be abundant on Mercury. The enstatite on the other hand does contain a considerable amount of iron in terms of weight percent. However, as it is heavier than Si and Mg (atomic mass of ≈ 56 compared to ≈ 28 and ≈ 34, respectively), the Fe contamination given in atomic percent is deemed acceptable. Moreover, despite the investigations concerning sputter yields and angular distributions of ejecta, this minor Fe content provides the possibility to study other space weathering phenomena such as the the formation of iron nanoparticles and the preferential implantation of solar wind ions therein [75].

A characterisation of the pellet samples is given in figure 4.2. Subfigures (a) and (b) show AFM images of the wollastonite and enstatite pellets, respectively. Figure 4.2c is a photo of a resulting pellet with a diameter of 1 mm inside the custom made stainless steel holder. Finally, figure 4.2d depicts the SIADs of the pressed pellets for both minerals. While the orange curve (wollastonite pellet) is almost identical to the inclination angle distribution of the corresponding thin film (figure 4.1), a deviating SIAD is observed for enstatite. Jäggi et al. reported in [69] that during the grinding of base material, needle-like structures formed in the wollastonite powder

due to it being a rather brittle material and due to well-developed cleavage. This provides a possible explanation for why the wollastonite pellets were smoother than the enstatite specimens. Due to the different roughnesses, a difference in sputtering behaviour can be expected when comparing the two enstatite sample configurations. Conversely, when only surface roughness effects are considered, no significant deviations in sputter yield and ejecta angular distribution are expected between the two wollastonite sample types.

4.4 Sample and Catcher Cleaning

Before every experiment, all samples were cleaned. Depending on the type of sample, a different procedure was used. However, most of the time sample preparation was carried out using sputtering by an ion beam. By means of the scanning electronics described in section 3.2, a suitable beam profile can be achieved. In preparation and experiment cycles, ion beams were used in three different geometries: focussed, scanned over a more narrow area of about $4 \times 4\,\mathrm{mm}^2$ and scanned over a wide area of roughly $8 \times 8\,\mathrm{mm}^2$. Beam geometry was probed using the Faraday Cup (see figure 3.2). It should however be kept in mind that the resulting profile is a convolution of the beam geometry and the FC aperture size. Therefore, to minimise the influence of this convolution effect, the wide beam profile was used to integrate the ion current density over the irradiated area. Figure 4.3 shows typical beam profiles (in this case of 4 keV He^+) in three geometries. Note that both the wide and narrow profile have been scaled by a factor of ten for the sake of visibility.

In order to clean the primary QCM, it was irradiated under an angle of incidence of 60°. Scanning was chosen to be wide in order to ensure homogeneous sputtering over the whole quartz area. The quartz resonance frequency was tracked and monitored. The sample was considered clean when a steady state sputter yield was reached. The transition from a dirty to a clean sample can be clearly observed due to the weak binding of physisorbed and chemisorbed adsorbates and contaminations. As long as these are present, sputter yields are typically heightened because the contaminations get sputtered more easily than actual sample material. The time necessary to achieve steady state sputtering was tracked.

Cleaning of the pellet sample was carried out in a similar fashion. However, no primary information on when the sputter yield has stabilised is available for this sample type. Therefore, the following assumption was made: Because both pellet and thin film were exposed to pollutants for the same amount of time and have the same stoichiometry, they are expected to be similarly contaminated. This is valid if both samples had been previously cleaned and were stored in UHV conditions. Therefore, the same fluence is necessary. Pellets were irradiated using a narrowly scanned beam profile in order to avoid sputtering of the sample holder, which could lead to contaminations with holder material on the pellet. As a result, the ion flux density was increased and therefore, irradiation time was reduced compared to the QCM cleaning to achieve the same fluence. Additionally, to counteract charging up of

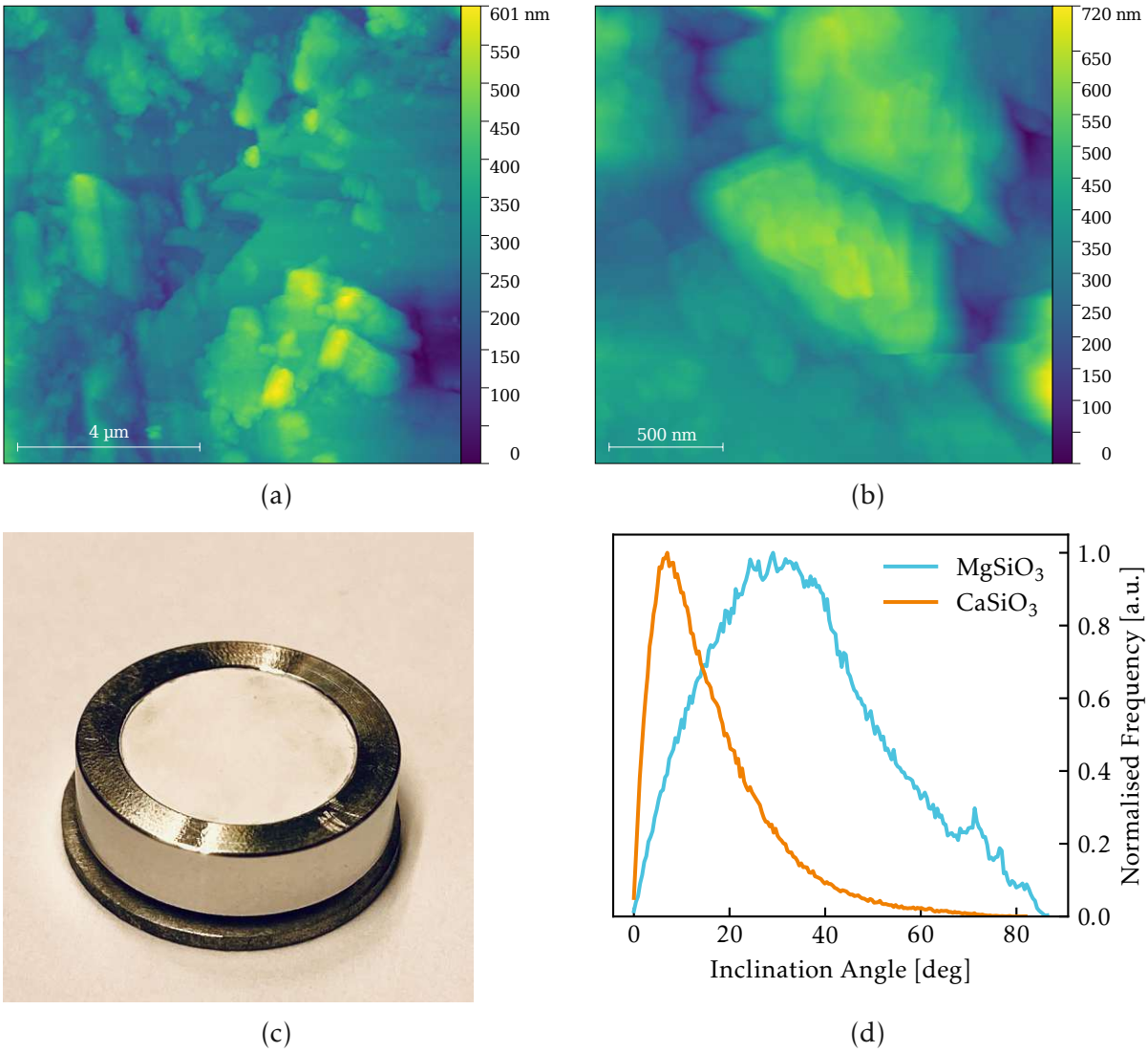

Figure 4.2: (a): AFM image of a wollastonite pellet.
(b): AFM image of an enstatite pellet.
(c): Photo of a mineral pellet pressed into a stainless steel holder.
(d): SIADs of pellets from both investigated sample minerals.

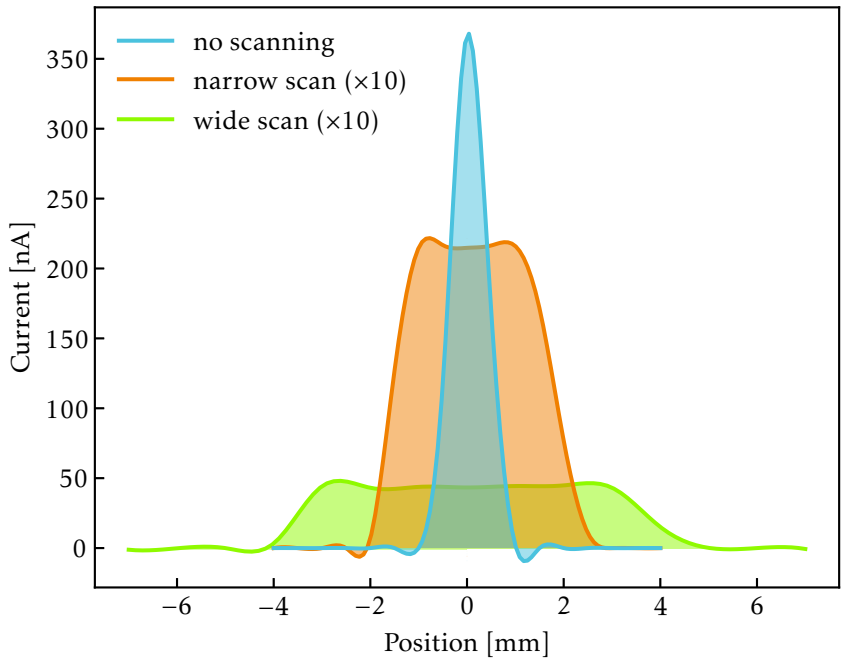

Figure 4.3: Various beam profiles achieved with scanning electronics and used for both sample preparation and sputtering experiments. Measured with the FC whose aperture size is 0.6 mm^2. Note the scaling by a factor of ten for the narrow and wide beam profiles.

the pellet, the electron flood source was active, providing 300 µA of 10 eV electrons.

This sputtering approach however produces ion beam damages like amorphisation in the topmost sample layers. While this is no problem for the thin films that show no crystal structure anyway, it might hinder investigations where fluence dependent effects of crystallinity are the main focus. Therefore, a second method of pellet cleaning was applied. The pellet was heated to roughly 330 °C and kept at this temperature for 6000 s to facilitate the desorption of contaminants. Moreover, 20 eV electrons were supplied to the sample. It has been reported that low energy electrons (≤ 20 eV) can lead to the desorption of adsorbates via so-called Electron Stimulated Desorption (ESD), more specifically through dissociative attachment mechanisms [76]. Because no direct information on the cleanliness of the pellet is available, this procedure was tested on a QCM where a steady state sputter yield indicates a clean surface. After the above described heat ramp and irradiation with low energetic electrons, indeed stable sputtering was found. It can therefore be concluded that cleaning through heating and ESD provides a feasible method of sample preparation for future measurements investigating crystallinity effects.

Due to the geometry of the setup, the catcher can only be cleaned under normal ion beam incidence. This is the only position on its arc where it is in the ion beam trajectory. Again, its resonance frequency was tracked and the catcher was considered clean when a steady state sputter yield was reached.

Sputter cleaning was carried out most of the time with a 2 keV Ar^+ ion beam for all samples. The only exception to this are measurements using a 4 keV He^+ ion beam. Samples for these specific experiments had also been cleaned with Ar after their initial installation into the vacuum chamber. However, once the ion species was switched to He, the chamber was not opened again and the only source of contamination was residual gas rather than air. It was therefore deemed sufficient to prepare the samples using the same He beam with which the experiments were conducted, also for time reasons. Changing the beam to Ar for cleaning and subsequently back to He would have taken one half up to a whole day and therefore, the specimens would have faced residual gas pressure for a significant amount of time. Operation of SOPHIE using a mixed gas plasma is possible and would have reduced beam switching times, but leads also to a decrease in available current for each ion species which in turn reduces the signal to noise ratio on the catcher.

4.5 Towards Quantifiable Systems Using Pellet Edge pre-Coating

As was reported in [77], a problem that was encountered in the past using this setup was that catcher signals varied by up to a factor of two between experiments under otherwise same conditions. Scaled results between measurement cycles, however, still showed qualitatively same behaviour.

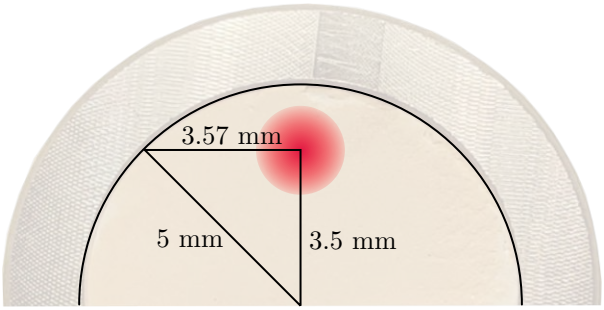

Figure 4.4: Geometry of the PEPC procedure. The semicircle represents the upper half of the pellet as is shown by the transparent photo background. The focussed ion beam hits the pellet 3.5 mm above its centre, away from the area usually irradiated during experiments and far enough from the edges so that no sputtering of the target holder occurs.

A first point of investigation concerned experimental geometry as the cacher configuration is very sensitive to changes in the target-catcher distance r (see figure 2.1). However, considering the $1/r^2$ behaviour of particle flux intensity, r would have to vary by $\sqrt{2}$ to explain the fluctuations by a factor of 2. At the nominal $r = 17\,\text{mm}$, this would mean geometric variations by $\approx 3\,\text{mm}$. Such large uncertainties in the experimental geometry are impossible due to the interconnected target and catcher holders. Additionally, experiments were carried out varying r by up to 1 mm. This value was chosen as an upper limit to estimate possible geometrical variations. Deviations were found between individual irradiations, however not by the amount that was to be explained. Geometry of the setup was therefore ruled out as a cause for these fluctuations.

Another possible explanation for this undesired behaviour were fluence dependent sticking probabilities on the catcher QCM. Therefore, a procedure was derived called Pellet Edge pre-Coating (PEPC, pronounced like the soft drink) and added to the catcher preparation cycle. The goal was to deposit sufficient material onto the catcher such that a steady state composition is achieved and no more fluence dependent sticking changes occur. The focussed beam is directed onto a spot near the pellet edge where no irradiation takes place during actual measurements. This spot is located 3.5 mm above the pellet centre. In the same direction, the irradiated rectangle stops at 2 mm above pellet centre. The geometry is sketched in figure 4.4. The red circle represents the ion with a radius of 1 mm where it decays to zero. This radius was estimated using the blue beam profile in figure 4.3. However, at this distance the *convolution* of both beam and FC geometry vanishes. It provides therefore an upper limit for the actual beam radius. Thus, a spot is found where it is ensured that neither the investigated area nor the sample holder are irradiated during PEPC. Also under incidences with $\alpha > 0°$, where the red circle in figure 4.4 becomes an ellipse, this condition is maintained due to sufficient space on the sides of the beam spot.

In the pre-coating procedure, multiple irradiations under the same conditions (incidence angle $\alpha = 45°$, catcher angle $\alpha_C = 25°$) are carried out. The resulting slopes of the catcher resonance frequency curves are plotted in figure 4.5 for two different catcher materials. The blue dots denote signals that were recorded using an Au coated QCM as catcher. Previously, a catcher that was coated with the same material as the samples to be investigated had been used. The intention thereof was to use a system which had similar stoichiometry compared to the particle flux to be caught. This did not mitigate however the deviation of absolute catcher signals. Therefore, a mono-elemental catcher appeared to be a step towards a more simple system. The resulting Au catcher slopes, however, scatter a lot. In fact, almost no material stuck to the catcher at all such that no difference in steepness could be observed. The given data points are the result of a drift compensation process in which the slope during an irradiation is corrected by subtracting the average slope of the quartz frequency drift immediately before and after the beam-on phase. For the Au catcher, slopes could not be distinguished from time spans where no irradiation took place and therefore, drift compensation proved useless; especially the negative data points are unphysical. The attempt in using a gold coated catcher QCM was thus considered failed.

On the other hand, the use of Fe as a single-component catcher coating seems more promising. Such iron coated QCMs were used in past investigations in the context of nuclear fusion research. A resonator with an already deposited Fe film like the ones used in [40] was therefore readily available. Again, PEPC was carried out and the resulting signals are given in figure 4.5 by the orange symbols. Both PEPC procedures with Au and Fe were conducted with similar current densities, therefore no normalisation per incident current was necessary for the direct comparison between the different coatings. With iron, an increase in slope is observed for the first three irradiations. For further irradiations, signals do not scatter significantly any more. To illustrate this, the average signal was calculated, taking only irradiations labelled 3-9 into account where signals were mostly stable. This average is plotted using the dashed line and the interval ±10% is shaded in light-orange. It is apparent that after the initial phase, where fluence dependence of the catcher signal is observed, no more significant variation of the data occurs as every data point lies within the 10% interval around this average. As other uncertainties in the setup (e.g. current uncertainties) are in a similar range, these fluctuations are deemed acceptable. More importantly, PEPC cycles were performed across multiple experimentation days and results were not only qualitatively, but also quantitatively comparable and well within their error bars. It is therefore concluded that through the use of an Fe coated QCM as catcher, the experimental setup is now under control to an extent that allows for quantifiable results using the evaluation approach described in section 2.2.

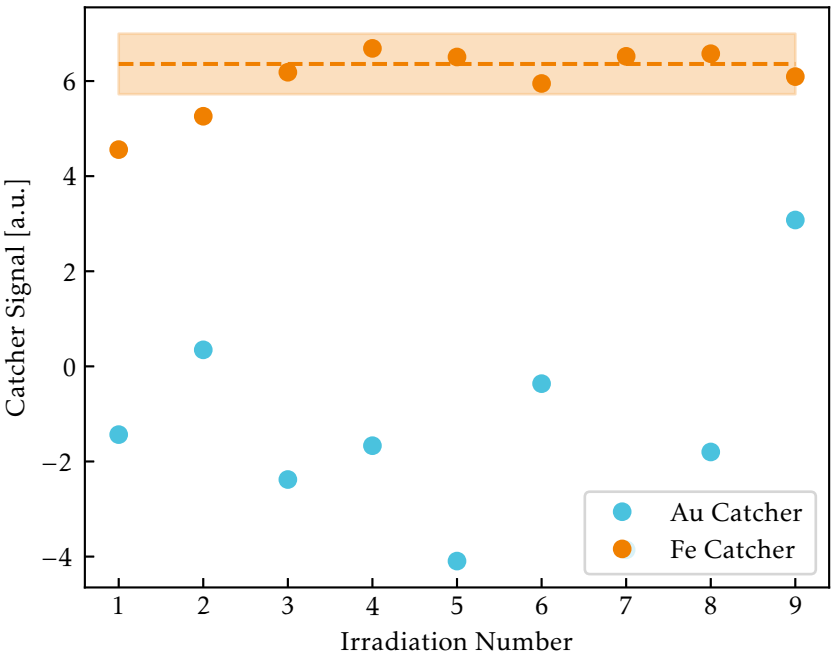

Figure 4.5: Comparison of two different materials for thin films on the catcher QCM. While gold shows a behaviour that is unusable for experiments because of very low sticking, the iron coated QCM presented stable enough slopes to be able to reproduce experiments.

4.6 Data evaluation

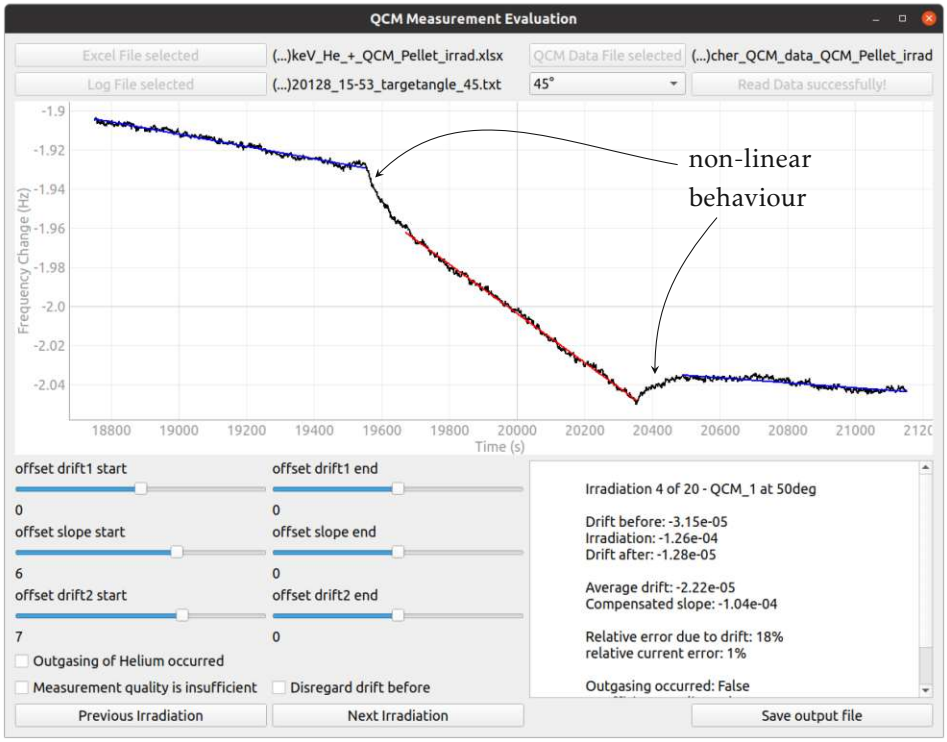

Figure 4.6: A screenshot of the newly developed data evaluation program. The depicted data show the necessity to adapt fitting parameters individually (see the annotated curves at the beginning and end of the fit plotted in red). This can be done by the sliders on the bottom left.

As discussed in section 2, the directly measured quantity of interest is the resonance frequency over time $f(t)$ of a quartz resonator. Its slope during time spans of irradiation can be obtained by means of a simple linear fit due to the linear nature of the Sauerbrey equation 2.1 and the expected constant mass change rate. For most of the measurements, this can be be automated by feeding the frequency data, starting time and end time of the irradiation into an analysis script. Uncertainties are mainly dominated by drifts in the quartz resonance frequency and changes in the ion beam current density. Both of these quantities enter equation 2.8 multiplicatively. The frequency drift can be averaged from the stints before and after a measurement and is subsequently subtracted from the slope. The average drift relative to the corrected slope and the relative deviation in ion beam current density are therefore considered in the error bars when the results are discussed in section 5. Both sources of errors can again be estimated automatically for each measurement cycle.

However, this approach was not applicable for all irradiation scenarios. Often, the slopes were not linear in the beginning (see figure 4.6), which might be related to implantation of reflected projectiles. A steady state was typically reached after about

200 s. These cases also showed an increase in $f(t)$ after the beam was turned off, indicating outgassing of the remaining ions. Nonetheless, this time varied at every investigated position α_C and therefore, automated evaluation could not be carried out. Measurements where this behaviour occurred are reported in section 5.3.

A tool was developed to sequentially show measurement points of the catcher resonance frequency and allow for individual adaptation of the fitting parameters. A screenshot with a representative frequency curve is given in figure 4.6. In the upper half, measurement data are plotted, while in the lower half sliders allow to shift the starting and end points of the linear fits. The plot and the information in the text box on the right-hand side are updated in real time. Moreover, a tagging of data points is possible to sort out measurements of insufficient quality. The output is then a list of slopes and, additionally, estimations of errors both due to resonance frequency drift and ion beam current uncertainties. It has to be kept in mind, however, that the resulting slopes are caused by absolute mass changes; not only by sputtering, but also by implantation and outgassing of ions themselves [78].

5 Results and Discussion

5.1 Ar^+ on Wollastonite ($CaSiO_3$)

Measurements with wollastonite were the first experiments performed since the setup was upgraded from the linear catcher geometry described in [54] to the herein described circular one. The sputtering behaviour of primary wollastonite coated QCMs was already extensively studied in, e.g. [18, 25, 79]. It was therefore considered a reasonable choice to test the capabilities of the system. The first measurements using an Ar^+ ion beam and their results were reported in [80]. However, data showed significant fluctuations of up to a factor of two between experiments performed on different days without PEPC as discussed in section 4.5. Thus, quantification of their results as sketched in section 2.2 did not yield consistent values. While these deviations between experimental cycles incited the investigations on how to simplify the setup and obtain reproducible results, the data still allows to draw qualitative conclusions using a slightly different approach in data evaluation.

Section 4.5 showed that some amount of material needs to be deposited onto the catcher QCM such that a steady state is reached. Wollastonite measurements were carried out before the introduction of PEPC, however. Catcher preparation consisted only of sputter cleaning the C-QCM. Moreover, a quartz resonator coated in wollastonite as opposed to a simple mono-elemental system was used as catcher. The freshly cleaned catcher surface seems to have demonstrated different sticking probabilities across experimentation cycles, and therefore catcher signals fluctuated. These sticking probabilities could be a stochastic quality of the QCM or, more likely, may have resulted from cleaning procedures where sputtering was interrupted too soon, caused by impatient experimenters. A more detailed investigation of the old data revealed that individual irradiations of samples during *a single measurement run* were kept short enough that the given sticking probabilities did not appear to have changed significantly. This allowed not only for qualitative comparison of data once they were appropriately scaled, but also to determine sputter yields of the pellet. These can be evaluated by comparing the pellet and QCM signals, as will be discussed in the next section 5.2.

The catcher's change in resonance frequency was not only normalised per incoming ion. Rather, sets of data obtained from pellet and QCM irradiations performed in the same measurement cycle were additionally scaled to each other using a single scalar value. In other words, it was examined how the angular distribution of particles sputtered from the mineral pellet behaved relative to the one of ejecta from the thin film on the primary QCM. This is possible because sputtering of $CaSiO_3$ films is

well-studied and excellent agreement in description of the sputter yield had already been established between experiments and SDTrimSP simulations [25]. Using this approach, the resulting signals were well comparable.

For irradiations under 45° incidence, a maximum of the angular emission characteristic was found around 40° ± 10° for both the amorphous film and the pellet as samples. Moreover, the relative intensities of their respective emission characteristics are well within the errors of each other. The match of both form and height indicates the same sputtering behaviour between the two sample configurations. This finding is supported by the measurements of Ar^+ impinging on wollastonite under 60° incidence. Again, both angular distribution and relative intensities between sample types match. As discussed in [29], the mean of the distribution of local surface inclination angles (SIAD) is a robust single parameter to describe the role of surface roughness in sputtering of real and stochastically rough surfaces. The SIADs of both types of wollastonite samples are almost identical (compare figures 4.1d and 4.2d). It is thus concluded that the geometric effects of their respective surfaces are enough to describe their coinciding sputtering behaviour. No additional parameters are necessary, indicating that for this set of samples, no influence from the polycrystallinity of the ground pellet is observable. It is therefore deduced that previous studies using the amorphous $CaSiO_3$ film as a model system for celestial body regolith material are validated. The vitreous films are in fact feasible specimens for this material and no additional information is gained when the pellets are used.

5.2 Ar^+ on Enstatite ($MgSiO_3$)

For measurements with enstatite, efforts were made to eliminate the above described deficiencies and therefore to allow direct quantification of results. PEPC was employed and an iron coated resonator was used as catcher, as described in section 4.5. Resulting data for a 2 keV Ar^+ beam under 60° incidence are shown in figure 5.1. These data were taken 14 days apart from each other. In the polar plot, the radial coordinate gives the mass deposited onto the catcher QCM normalised per incoming ion and per solid angle. The angle α_C is defined as the relative angle between the target and catcher surface normals as depicted in figure 2.1. Positive values denote the forward direction and therefore, the incoming ion beam is marked as coming from the left at -60°.

It is evident from the plot that for both measurement cycles, the reported catcher yield values $y_{C,\Omega}$ between the different days are well within the error bars of each other for both sample configurations, pellet and thin film. This is considered a success of the improved setup and catcher preparation and is explicitly shown here to show the reproducibility of the experiments.

Qualitatively, the smoother PLD film on the QCM shows a pronounced angular characteristic in forward direction with a maximum located at around $\alpha_C = 30°$ relative to the target surface normal. For this catcher angle, about 27 amu stick to the catcher per incident ion and steradian. When irradiating the pellet, a different

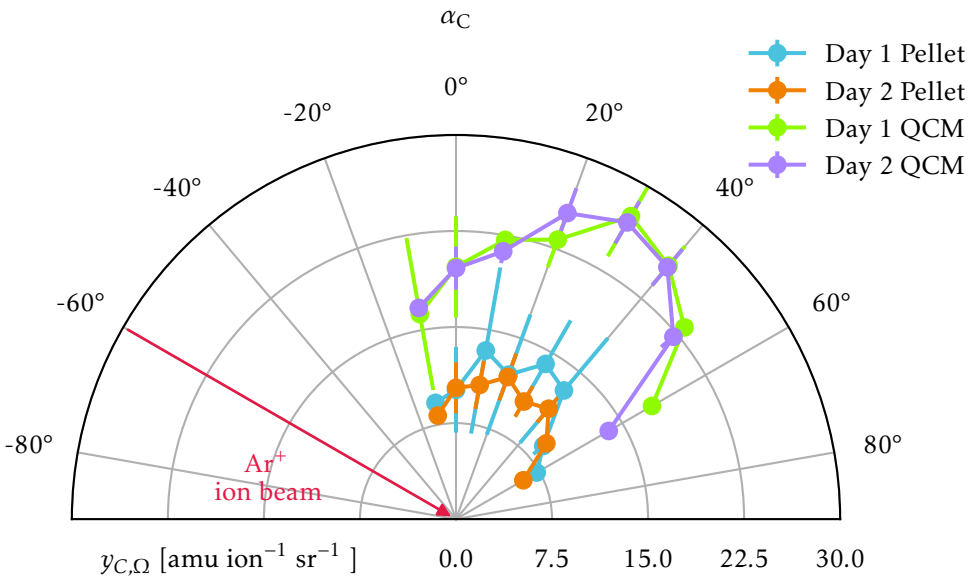

Figure 5.1: Angular distributions of ejecta sputtered by 2 keV Ar^+ ions from enstatite. Agreement between measurements performed on different days can be seen. A pronounced peak in forward direction is observed for bombardment of the thin film, whereas the distribution of the pellet is both dampened and exhibits less dependence on the catcher angle α_C.

situation is found. Not only is the signal reduced to about 10 amu ion^{-1} sr^{-1}, but also the angular characteristic is smeared out. Almost constant values are reported for α_C in the range from 20° up to about 50° and only for even bigger angles a decrease in the catcher yield is resolved. This is very well within the expectation and can be attributed to roughness effects. It has been shown that for rough surfaces, the sputter yield as a function of ion beam incidence angle is increased for smaller angles while it is lowered for larger ones (e.g. the here investigated 60°), depending on the roughness regime [41]. Therefore, its maximum is flattened. Because the pellet is significantly rougher than the glassy film as characterised by their respective local inclination angle distribution (see figures 4.2d and 4.1d), this decrease in mass deposited onto the catcher can be ascribed to their different surface roughness. Additionally, the angular distribution of ejecta is averaged over due to a rough surface showing facets oriented in multiple directions. This effect is observed in the dampening of the peak in the forward direction.

This argument is also consistent with the results found for irradiation under 45° depicted in figure 5.2. Here, a similar angular characteristic is seen for irradiation of the film sample as was observed under 60° impingement. However, the maximum is reduced to about 16 amu ion^{-1} sr^{-1}, qualitatively corresponding to the expected decrease in sputter yield of a flat surface when the incidence angle is reduced from 60° to 45° (see, e.g. the solid line in figure 5.3).

An attempt in quantifying the total sputter yield from the pellet is made by comparing the catcher signals for the different sample configurations, such that

$$Y_{\text{Pellet}} = r \cdot Y_{\text{QCM}}\,. \tag{5.1}$$

Here, Y denotes the total sputter yield and r gives the relative proportion between the yields of the respective sample types. Because Y_{QCM} is known from direct thin film irradiations, Y_{Pellet} can be obtained for an experimentally evaluated r. It can be interpreted as a weighted average of the data points using

$$r = \frac{1}{\sum_j y_{\text{C,QCM,j}}} \sum_i \cancel{y_{\text{C,QCM,i}}} \frac{y_{\text{C,Pellet,i}}}{\cancel{y_{\text{C,QCM,i}}}} = \frac{\sum_i y_{\text{C,Pellet,i}}}{\sum_i y_{\text{C,QCM,i}}}\,. \tag{5.2}$$

In the sum over i, the rightmost term gives the relative intensity of a single data point obtained from pellet irradiation compared to thin film irradiation. This fraction is then weighted with the corresponding data for the film irradiation such that data points for higher mass deposition contribute more to the average. Finally, the sum over j is there to normalise this weighted average. Of course, inside the summation over i, the QCM data points just cancel such that r can be obtained as the ratio of summed data points for the different sample types. This works if for both sample configurations, the same catcher angles α_C were probed in the same steps along the catcher arc. This also corresponds to a discretised integration and the ratio of the areas under these angular distributions.

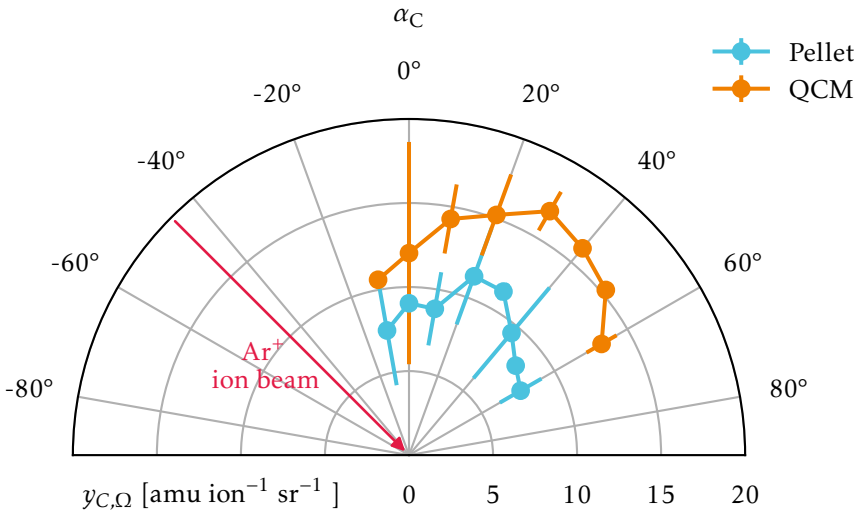

Figure 5.2: Catcher yield $y_{C,\Omega}$ for 2 keV $Ar^+ \rightarrow MgSiO_3$ as a function of the catcher angle α_C. The curve for the thin film has a similar qualitative behaviour as for irradiation under 60° incidence, is however decreased in terms of absolute numbers. Results for pellet irradiation remain almost the same under this reduction of incidence angle.

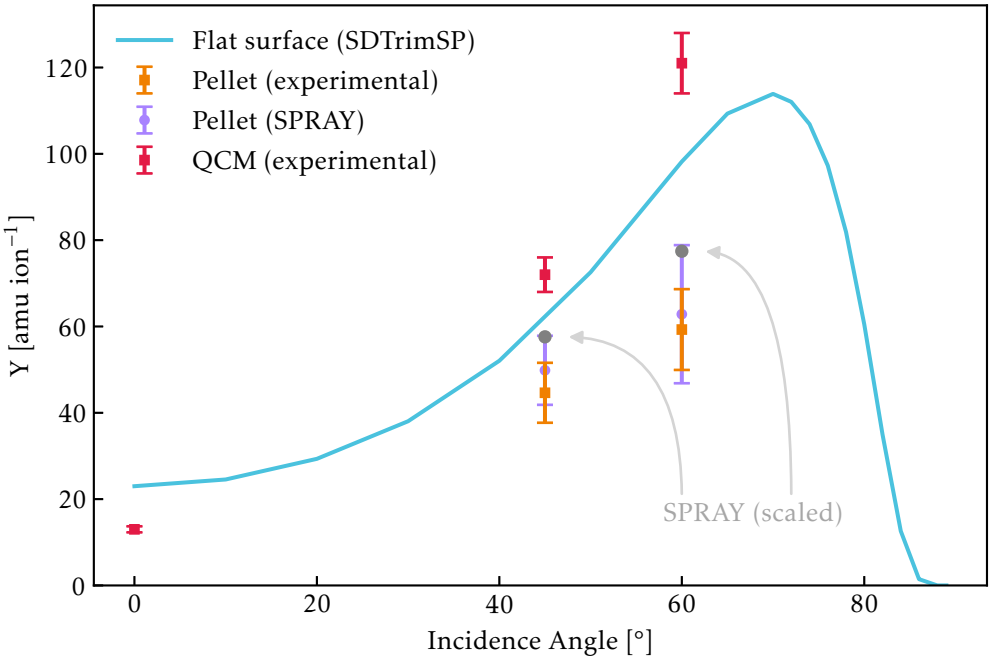

Figure 5.3: A summary of the sputter yields obtained for 2 keV Ar^+ irradiation of enstatite. Shown are the expected results for a simulated flat surface and the experimental results for both the pellet and thin film sample type.

The evaluated sputter yields for the pellet specimen are depicted in figure 5.3 in combination with their counterparts directly measured from (flat) vitreous film irradiation. Also shown are the SDTrimSP simulation for a perfectly flat surface and SPRAY simulation results for the pellet. SPRAY was not performed for the thin film samples as their roughness is small enough that only minor differences compared to artificial flat surfaces are to be expected [29].

In figure 5.3, the blue solid line gives the simulated sputter yield of 2 keV Ar^+ on enstatite as obtained by SDTrimSP simulations. It is important to note that input parameters, especially the surface binding energy of O, have been adapted to the same values as described in [18]. There is a slight underestimation of the experimentally found values shown by the red boxes. On the other hand, without this adjustment, the simulation would overestimate the measured data. As the changes in surface binding energy were fitted to match wollastonite [18], it is likely that parameters can be found to achieve better agreement for the here presented enstatite data. It is however not the goal of this thesis to find yet another fitted binding energy. Simulation of the sputtering of minerals is currently under active investigations and better systematic ways of description might emerge soon [44, 81].

Also, experimentally obtained r ratios (see equation 5.1) for pellet irradiation deviate by about 23% from the ones given by SPRAY simulations. The relative overestimation of the SPRAY code is the same for both investigated incidence angles. This coincidence of relative discrepancies could indicate some systematic shortcomings in the simulation code in the sense that some physical aspect of the sample-ion interaction is not featured. These include the negligence of ion implantation or the lack of consideration of expected ion penetration depths. However, as the penetration depth of 2 keV Ar^+ on enstatite is about 3 nm (see figure 5.4b), these effects are not considered limiting in the presented case study for Ar on $MgSiO_3$. It is more likely that the matching deviation of 23% in the obtained r ratios is coincidental and differences between experiment and SPRAY simulation stem from experimental uncertainties. Moreover, AFM images that serve as input for SPRAY cover surfaces of roughly some μm^2 whereas the irradiated area on the samples is in the order of mm^2. Of course, several spots have been measured, simulated and averaged over. Nonetheless, at this stage biassing might have occurred. Factors limiting the accuracy of the experimental setup are the rather coarse scanning of catcher angles due to the finite size of the catcher QCM or the incomplete coverage of solid angle by the catcher due to shadowing of the ion beam in the negative α_C range. Moreover, with the experimental setup only a slice in the plane spanned by the incidence beam and sample surface normal is taken out of the 4π solid angle. SPRAY simulations, on the other hand, consider the particles sputtered in all directions. This effect is also encountered when irradiating the vitreous thin film instead of the pellet. However with rougher samples, that smear out the angular emission characteristic, it is more pronounced. Therefore, for pellet specimens especially, this poses another point to consider when directly comparing experiments with SPRAY data.

Sputter yield ratios for the two sample types at each incidence angle deviate between experiment and simulation. However, when computing absolute pellet sputter yields rather than ratios according to equations 5.1 and 5.2, different Y_{QCM} are assumed: either directly measured for the experimental values or simulated from SDTrimSP. While SDTrimSP underestimates primary sputter yields when using the adaptations from [18], SPRAY overestimates the r ratios compared to the experiment. The total Y_{Pellet}^{SPRAY} (purple circles in figure 5.3) as a multiplication of both therefore matches quite well with the purely experimental results (orange squares in the same figure). It is emphasised that this match happens most likely by chance and the almost excellent agreement between simulated and measured values is not systematic. To highlight this, another data set is shown and annotated in figure 5.3. The grey circles represent the r values obtained by SPRAY, but scaled with the experimentally measured primary yields for the film on the QCM rather than the simulated ones. This highlights the deviations between experiment and simulation in order to not just show possibly deceitful and coincidental agreement.

Nonetheless, the trend of the experimentally obtained values is reproduced by the simulation taking into account only geometric effects of the sample surface roughness. Moreover, the displacements per atom (dpa) that the Ar beam causes extend into the bulk in the range of about the penetration depth (see figure 5.4c). Therefore,

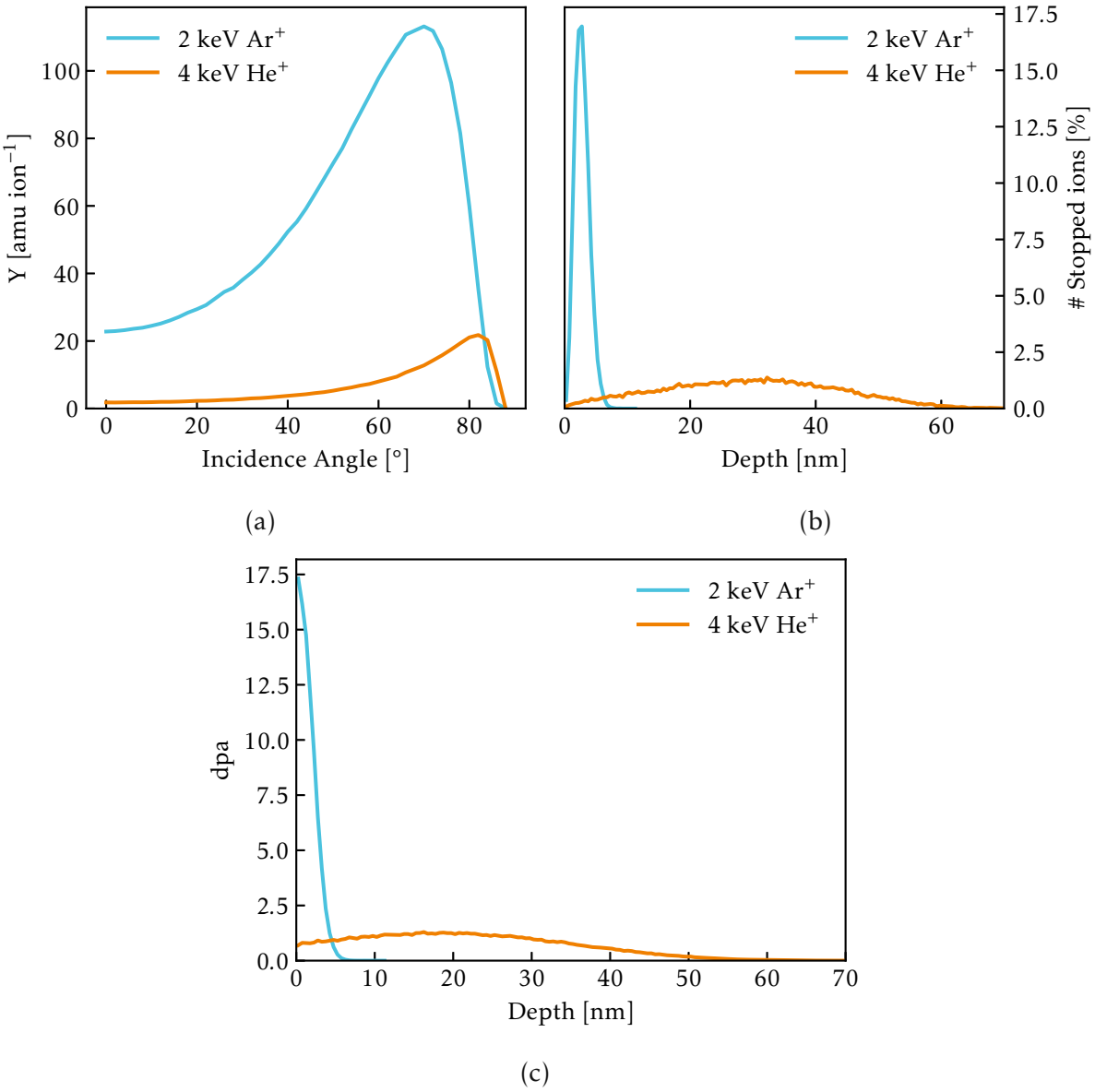

Figure 5.4: (a): Sputter yield as a function of incidence angle for both Ar and He on enstatite.
(b): Implantation depths for both species given by the number of stopped ions over target depth as a percentage of the total number of simulated ions.
(c): Number of displacements per atom (dpa) for Ar and He on enstatite.
All data obtained from SDTrimSP. Figures (b) and (c) were simulated for normal incidence, figure (c) depicts damages as caused by a fluence of 0.5×10^{20} ions m^{-2}.

amorphisation is caused deeper in the bulk than the top surface where a significant fraction of sputtered material comes from [81]. Crystallinity thus does not seem to affect the measurements presented in this section and sample roughness alone is a robust predictor of the sputtering behaviour.

5.3 He^+ on Enstatite ($MgSiO_3$)

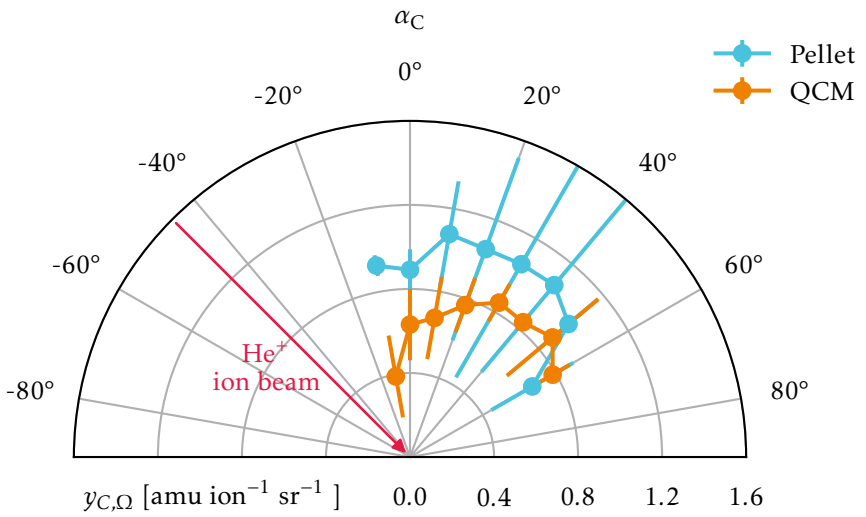

Figure 5.5: Catcher yield $y_{C,\Omega}$ for 4 keV $He^+ \rightarrow MgSiO_3$. Curves for both the vitreous film on a QCM and mineral pellet are mostly within the (large) error bars of each other. As opposed to the Ar measurements, signals for pellet irradiation are higher than for the film. In the forward direction at about $\alpha_C \approx 45°$, signals cannot be attributed to merely ejecta deposition anymore. Rather, implantation of reflected ions has to be considered.

When switching the ion beam from 2 keV Ar^+ for proof of principle measurements to solar wind relevant ions and energies (4 keV He^+), some further hardships emerged. Especially in the forward direction where the catcher angle roughly equalled the ion beam incidence angle ($\alpha_C \approx \alpha$, see figure 2.1), slopes of the catcher resonance frequency were not linear. About 200 s were necessary until steady state behaviour and linear slopes were recovered in most instances. As this behaviour however depended on the catcher position α_C, every time span of irradiation in the catcher resonance frequency had to be evaluated individually in order to find starting and end points for which a linear fit was feasible. This was done in accordance with the description in section 4.6.

This effect occurred mainly with catcher angles in forward direction, $\alpha_C \geq 45°$. In this angular regime, a faster than linear decrease of the catcher resonance frequency was observed in the beginning of an irradiation as well as an increase of $f(t)$ when the beam was switched off. This can be seen in the screenshot in figure 4.6 where the corresponding points are annotated by the arrows. The same behaviour using a He beam was discussed and studied in [18, 78]. It is therefore ascribed to the implantation and outgassing of reflected He ions at the beginning and ending of the irradiation time span, respectively.

Keeping these effects in mind, results from first He on $MgSiO_3$ measurements are shown in figure 5.5. Due to time constraints and the above described initial complications when working with He, only one usable data set could be obtained so far. Note that the scale of the radial axis is reduced by factor of about 10 compared to the Ar measurements in the previous section 5.2 with the same ion impact angle of 45°. This reduced sputter yield can be ascribed mostly to the lighter projectile mass and therefore the reduced momentum and energy transfer to the target atoms. A comparison of simulated sputter yields between 2 keV Ar^+ and 4 keV He^+ is given in figure 5.4a.

Another difference from Ar irradiations is given by how close the signals from pellet and thin film samples are to each other. In fact, more mass was deposited onto the catcher from pellet irradiations. However, error bars are rather large due to high ion current uncertainties during this particular measurement. Due to these large uncertainties, no clear statement can be made whether the pellet gives truly higher signals, but a reduction as was observed for Ar can most likely be excluded. This point will be investigated in the near future when more data with better statistics are available. For now, the reported mass depositions are considered roughly equal for both sample types.

A possible explanation for this behaviour is proposed as the following working hypothesis: Due to the larger penetration depth of the He ions compared to Ar (see figure 5.4b), size scales of the collisional cascade inside the solid are bigger for this ion species. Therefore, the size of the rough features on the pellet surface relative to this cascade are reduced. Effectively, it could be that the incident beam cannot resolve the surface roughness of pellet with such high resolution as the Ar projectiles and thus, it could appear smoother to the He ions. To check whether this is the case, simulation results of SPRAY (purely geometric and neglects collision cascades) could be compared to codes like SDTrimSP-3D. These are not restricted solely to surface geometry, but truly take the interaction of ions with the whole surface and bulk underneath into account. So far, this comparison has not been done and further research is still necessary.

Not discussed so far are effects on the sputter yield by the polycrystallinity of the mineral pellets. As can be seen in figure 5.4c, the ion beam damages caused by He irradiation in the form of displacements per atom extend much farther into the bulk compared to Ar. However, they are not as numerous in the upper sample layers. Therefore, amorphisation of the sputtered surface area cannot be assumed as easily as was done for Ar irradiations in section 5.2. As long as not a sufficient amount

of damages has occurred to amorphise the enstatite, a fluence dependent effect of crystallinity, grain sizes or orientation of grains could be observed in addition to geometrical surface roughness influences. In the literature, a threshold value of an ion fluence of $(1-5)\times 10^{20}\,\mathrm{ions\,m^{-2}}$ is given until the surface layer of olivine, a magnesium iron silicate, is totally amorphised due to 4 keV He^+ ion irradiation [82]. In the laboratory using the SOPHIE ion source, this fluence is reached already after one or two measurement cycles, depending on the amount of catcher position per cycle and taking into consideration the longer irradiation times necessary until a steady state on the catcher is reached. Therefore, an amorphous surface layer is expected on the pellet in a timescale that is short enough to thwart simultaneous investigation of both the ejecta angular distribution and crystallinity effects.

A similar situation is found in space. On the Moon, craters of about 8 cm diameter are turned over, on average, in about 10^6-10^7 years, whereas depths of 0.1 mm are turned over about five times in 10^4 years [83]. The Apollo 15 mission reported ^{4}He fluxes in the range of $10^{10}\,\mathrm{m^{-2}\,s^{-1}}$ [84]. This means that the above mentioned fluence is reached for the smaller grain size in roughly 300 years. Therefore, a grain of lunar regolith will have a completely amorphous surface before it is excavated and a still crystalline facet faces the solar wind. In the context of space weathering it is thus sufficient to probe the angular distribution of ejecta in order to determine sputter yields for the pellet samples. This can also be done with an already amorphous sample, for which measurements can be repeated to achieve better statistics.

Once suitable and stable experimental settings are found through these experiments, it is conceivable that crystallinity effects are investigated in the future. This would have to happen with a single fixed α_C, however. A virgin pellet that has not been exposed to any ion beam fluence is to be used, making the preparation procedures derived in this thesis (pellet cleaning without sputtering and PEPC, see sections 4.4 and 4.5, respectively) all the more important.

6 Conclusion and Outlook

In this work, an advanced QCM measurement technique was employed to shed light on the contribution of solar wind sputtering to the formation of exospheres around rocky bodies in space without protective atmospheres. Not only can sputter yields of thin films deposited on a QCM be determined *in situ* and in real time, but by means of second microbalance information about bulk targets made of compressed mineral powder was obtained. A direct comparison of sputtering behaviour of thin vitreous films and mineral pellets was therefore possible. While the films allow more straight forward evaluation of sputter yields, the pellets are a more realistic representation of Lunar or Hermean surface regolith. Wollastonite ($CaSiO_3$) and enstatite ($MgSiO_3$), two silicate minerals, served as analogue materials. They belong to the pyroxenoid and pyroxene families, respectively, which are expected to make up a large fraction of rocky material on both Mercury and the Moon.

With the focus on enstatite, an existing catcher QCM setup was improved to not only allow for qualitative, but also quantitative results. During the course of this optimisation process, several software tools were developed, giving rise to a high degree of automation and therefore fast working routines. Especially the graphical user interface for data evaluation was a crucial element due to the large number of data points and the necessary individual fitting. Using a preparation process in which sufficient amounts of sample material are deposited onto the catcher QCM, a steady state with no more fluence dependence of the catcher sticking probabilities was reached. The reproducibility of experiments was shown with 2 keV Ar^+ as a projectile. An explanation for the sputter yields was discussed to be possible from geometric considerations alone, taking into account different roughness scales characterised by their mean local inclination angle.

For experiments with a more solar wind relevant ion species, 4 keV He^+, additional hardships had to be overcome, thus limiting the amount of data available for discussion in this thesis. Nonetheless, first results are reported. A working hypothesis of ion species dependent effective roughness was put forth. However, an interplay of surface roughness and possible crystallinity could not be excluded. Amorphisation timescales were estimated to be in the same order of magnitude that is necessary to probe angular emission characteristics. More prolonged irradiations could make clear whether this assumption holds, and by relinquishing the probing of angular distributions, the unravelling of crystallinity and roughness could become possible.

In the near future, experiments with He will continue so as to obtain more precise data and to further investigate the above mentioned hypothesis. These measurements are of special interest as they are the most relevant in the context of space weathering so far. This is due to the combination of target material and ion species. They will

however be outperformed in their relevance by experiments with real Lunar regolith as a target material. Recently, 2.4 g of Lunar soil from the Apollo 16 mission were provided by NASA. These samples currently reside with collaborators from the University of Bern. There, first trials are currently being made to press them into pellets. Measurements with real Lunar regolith are expected to commence in the late upcoming spring or early summer of this year.

Bibliography

1. Grün, E., Horanyi, M. & Sternovsky, Z. The lunar dust environment. *Planetary and Space Science* **59,** 1672–1680 (2011).
2. Yakshinskiy, B. V. & Madey, T. E. Photon-stimulated desorption as a substantial source of sodium in the lunar atmosphere. *Nature* **400,** 642–644 (1999).
3. Hapke, B. Space weathering from Mercury to the asteroid belt. *Journal of Geophysical Research: Planets* **106,** 10039–10073 (2001).
4. McCord, T. B. *et al.* Moon: Near-infrared spectral reflectance, a first good look. *Journal of Geophysical Research: Solid Earth* **86,** 10883–10892 (1981).
5. Brunetto, R. & Strazzulla, G. Elastic collisions in ion irradiation experiments: A mechanism for space weathering of silicates. *Icarus* **179,** 265–273 (2005).
6. Wurz, P. *et al.* Self-consistent modelling of Mercury's exosphere by sputtering, micro-meteorite impact and photon-stimulated desorption. *Planetary and Space Science* **58,** 1599–1616 (2010).
7. Vervack, R. *et al.* Mercury's complex exosphere: results from MESSENGER's third flyby. *Science* **329,** 672–5 (2010).
8. Benkhoff, J. *et al.* BepiColombo—Comprehensive exploration of Mercury: Mission overview and science goals. *Planetary and Space Science* **58,** 2–20 (2010).
9. Orsini, S. *et al.* SERENA: A suite of four instruments (ELENA, STROFIO, PICAM and MIPA) on board BepiColombo-MPO for particle detection in the Hermean environment. *Planetary and Space Science* **58,** 166–181 (2010).
10. *BepiColombo's first views of Mercury* `https://www.esa.int/Science_Exploration/Space_Science/BepiColombo/BepiColombo_s_first_views_of_Mercury`. Accessed: 2022-02-27.
11. Stern, S. A. The lunar atmosphere: History, status, current problems, and context. *Reviews of Geophysics* **37,** 453–491 (1999).
12. Killen, R. M., Bida, T. A. & Morgan, T. H. The calcium exosphere of Mercury. *Icarus* **173,** 300–311 (2005).
13. Brueckner, G. & Bartoe, J. Observations of high-energy jets in the corona above the quiet sun, the heating of the corona, and the acceleration of the solar wind. *The Astrophysical Journal* **272,** 329–348 (1983).
14. Feldman, U., Landi, E. & Schwadron, N. A. On the sources of fast and slow solar wind. *Journal of Geophysical Research: Space Physics* **110** (2005).

15. Wimmer-Schweingruber, R. F. The composition of the solar wind. *Advances in Space Research* **30,** 23–32 (2002).

16. Bame, S. J., Asbridge, J. R., Feldman, W. C., Montgomery, M. D. & Kearney, P. D. Solar wind heavy ion abundances. *Solar Physics* **43,** 463–473 (1975).

17. Nénon, Q. & Poppe, A. R. On the Long-term Weathering of Airless Body Surfaces by the Heavy Minor Ions of the Solar Wind: Inputs from Ion Observations and SRIM Simulations. *The Planetary Science Journal* **1,** 69 (2020).

18. Szabo, P. S. *et al.* Dynamic Potential Sputtering of Lunar Analog Material by Solar Wind Ions. *The Astrophysical Journal* **891,** 100 (2020).

19. Hunten, D., Morgan, T. & Shemansky, D. The mercury atmosphere. *Mercury.* University of Arizona Press Tucson, 562–612 (1988).

20. Bida, T. A., Killen, R. M. & Morgan, T. H. Discovery of calcium in Mercury's atmosphere. *Nature* **404,** 159–161 (2000).

21. Burger, M. H. *et al.* Monte Carlo modeling of sodium in Mercury's exosphere during the first two MESSENGER flybys. *Icarus* **209,** 63–74 (2010).

22. Wurz, P. *et al.* The lunar exosphere: The sputtering contribution. *Icarus* **191,** 486–496 (2007).

23. Wurz, P. & Lammer, H. Monte-Carlo simulation of Mercury's exosphere. *Icarus* **164,** 1–13 (2003).

24. Ziegler, J. F., Ziegler, M. & Biersack, J. SRIM – The stopping and range of ions in matter (2010). *Nuclear Instruments and Methods in Physics Research Section B: Beam Interactions with Materials and Atoms* **268,** 1818–1823 (2010).

25. Szabo, P. S. *et al.* Solar wind sputtering of wollastonite as a lunar analogue material–Comparisons between experiments and simulations. *Icarus* **314,** 98–105 (2018).

26. Mutzke, A. *et al. SDTrimSP Version 6.00* Max-Planck-Institut für Plasmaphysik (2019).

27. Schaible, M. J. *et al.* Solar Wind Sputtering Rates of Small Bodies and Ion Mass Spectrometry Detection of Secondary Ions. *Journal of Geophysical Research: Planets* **122,** 1968–1983 (2017).

28. Hayderer, G., Schmid, M., Varga, P., Winter, H. & Aumayr, F. A highly sensitive quartz-crystal microbalance for sputtering investigations in slow ion–surface collisions. *Review of Scientific Instruments* **70,** 3696–3700 (1999).

29. Cupak, C. *et al.* Sputter yields of rough surfaces: Importance of the mean surface inclination angle from nano- to microscopic rough regimes. *Applied Surface Science* **570,** 151204 (2021).

30. Rainer Behrisch, W. E. *Sputtering by Particle Bombardment. Experiments and Computer Calculations from Threshold to MeV Energies* (Springer, Berlin, Heidelberg, 2007).

31. Sigmund, P. Theory of Sputtering. I. Sputtering Yield of Amorphous and Polycrystalline Targets. *Physical Review* **184,** 383 (1969).

32. Hotston, E. Threshold energies for sputtering. *Nuclear Fusion* **15,** 544–547 (1975).

33. Aumayr, F. & Winter, H. Potential sputtering. *Philosophical Transactions of the Royal Society of London. Series A: Mathematical, Physical and Engineering Sciences* **362,** 77–102 (2004).

34. Winter, H. & Aumayr, F. Hollow atoms. *Journal of Physics B: Atomic, Molecular and Optical Physics* **32,** R39–R65 (1999).

35. Sporn, M. *et al.* Potential Sputtering of Clean SiO_2 by Slow Highly Charged Ions. *Phys. Rev. Lett.* **79,** 945–948 (1997).

36. Wilhelm, R. A. *et al.* Highly charged ion induced nanostructures at surfaces by strong electronic excitations. *Progress in Surface Science* **90,** 377–395 (2015).

37. Aumayr, F., Facsko, S., El-Said, A. S., Trautmann, C. & Schleberger, M. Single ion induced surface nanostructures: a comparison between slow highly charged and swift heavy ions. *Journal of Physics: Condensed Matter* **23,** 393001 (2011).

38. Eckstein, W. in *Sputtering by Particle Bombardment. Experiments and Computer Calculations from Threshold to MeV Energies* chap. 2 (Springer, Berlin, Heidelberg, 2007).

39. Gnaser, H. in *Sputtering by Particle Bombardment. Experiments and Computer Calculations from Threshold to MeV Energies* chap. 4 (Springer, Berlin, Heidelberg, 2007).

40. Stadlmayr, R. *et al.* Fluence dependent changes of surface morphology and sputtering yield of iron: Comparison of experiments with SDTrimSP-2D. *Nuclear Instruments and Methods in Physics Research Section B: Beam Interactions with Materials and Atoms* **430,** 42–46 (2018).

41. Küstner, M., Eckstein, W., Dose, V. & Roth, J. The influence of surface roughness on the angular dependence of the sputter yield. *Nuclear Instruments and Methods in Physics Research Section B: Beam Interactions with Materials and Atoms* **145,** 320–331 (1998).

42. Malherbe, J., Hofmann, S. & Sanz, J. Preferential sputtering of oxides: A comparison of model predictions with experimental data. *Applied Surface Science* **27,** 355–365 (1986).

43. Eckstein, W. & Urbassek, H. M. in *Sputtering by Particle Bombardment. Experiments and Computer Calculations from Threshold to MeV Energies* chap. 1 (Springer, Berlin, Heidelberg, 2007).

44. Morrissey, L. S., Tucker, O. J., Killen, R. M., Nakhla, S. & Savin, D. W. Solar Wind Ion Sputtering of Sodium from Silicates Using Molecular Dynamics Calculations of Surface Binding Energies. *The Astrophysical Journal Letters* **925,** L6 (2022).

45. Onderdelinden, D. The Influence of Channeling on Cu Single-Crystal Sputtering. *Applied Physics Letters* **8,** 189–190 (1966).

46. Schlueter, K. *et al.* Absence of a crystal direction regime in which sputtering corresponds to amorphous material. *Physical review letters* **125,** 225502 (2020).

47. Thompson, M. W. II. The energy spectrum of ejected atoms during the high energy sputtering of gold. *The Philosophical Magazine: A Journal of Theoretical Experimental and Applied Physics* **18,** 377–414 (1968).

48. Szabo, P. *Experimental and Simulated Sputtering of Gold, Iron and Wollastonite with a Catcher-QCM Setup* MA thesis (TU Wien, 2017).

49. Möller, W. TRI3DYN – Collisional computer simulation of the dynamic evolution of 3-dimensional nanostructures under ion irradiation. *Nuclear Instruments and Methods in Physics Research Section B: Beam Interactions with Materials and Atoms* **322,** 23–33 (2014).

50. Arredondo, R. *et al.* Angle-dependent sputter yield measurements of keV D ions on W and Fe and comparison with SDTrimSP and SDTrimSP-3D. *Nuclear Materials and Energy* **18,** 72–76 (2019).

51. Brötzner, J. *A Catcher-QCM Setup for Measuring Sputtering Yields of Wollastonite as Hermean Surface Regolith Analogue* Project Work. 2021.

52. Sauerbrey, G. Verwendung von Schwingquarzen zur Wägung dünner Schichten und zur Mikrowägung. *Zeitschrift für Physik* **155,** 206–222 (1959).

53. Dobes, K. *Erosion of fusion relevant surfaces under ion impact* PhD thesis (TU Wien, 2014).

54. Berger, B. M., Szabo, P. S., Stadlmayr, R. & Aumayr, F. Sputtering measurements using a quartz crystal microbalance as a catcher. *Nuclear Instruments and Methods in Physics Research Section B: Beam Interactions with Materials and Atoms* **406,** 533–537 (2017).

55. Berger, B. *Laboratory work on plasma-wall-interaction processes relevant for fusion experiments* PhD thesis (TU Wien, 2017).

56. Galutschek, E. *Development of a 14.5 GHz all-permanent magnet multicharged ECR ion source for remote operation* PhD thesis (TU Wien, 2005).

57. Galutschek, E., Trassl, R., Salzborn, E., Aumayr, F. & Winter, H. Compact 14.5 GHz all-permanent magnet ECRIS for experiments with slow multicharged ions. *Journal of Physics: Conference Series* **58,** 395–398 (2007).

58. Berger, B. M. *et al.* Erosion of Fe-W model system under normal and oblige D ion irradiation. *Nuclear Materials and Energy* **12,** 468–471 (2017).

59. Szabo, P. *Novel Insights into Ion-Solid Interaction: Case Studies for Space Weathering and Nuclear Fusion Research* PhD thesis (TU Wien, 2021).

60. Holter, B. *Measuring sputter yields of Mercury analogues at different temperatures with a QCM* Project Work. 2021.

61. Johnson, V. R. & Vaughn, G. W. Investigation of the Mechanism of MoS_2 Lubrication in Vacuum. *Journal of Applied Physics* **27,** 1173–1179 (1956).
62. Biber, H. *Sputtering investigations of wollastonite using solar wind ions* MA thesis (TU Wien, 2018).
63. Lefebvre, L. *pyModbusTCP* `https://pypi.org/project/pyModbusTCP/`. Accessed: 2022-03-25.
64. Brötzner, J. *Development of a Graphical User Interface to remotely control Ion Beam Experiments* Project Work. 2022.
65. Hayderer, G. *Projectile charge state dependent sputtering of solid surfaces* PhD thesis (TU Wien, 2000).
66. *Python* `https://www.python.org/`. Accessed: 2022-03-25.
67. Stadlmayr, R. *et al.* A high temperature dual-mode quartz crystal microbalance technique for erosion and thermal desorption spectroscopy measurements. *Review of Scientific Instruments* **91,** 125104 (2020).
68. *LabView* `https://www.ni.com/de-at/shop/labview.html`. Accessed: 2022-03-25.
69. Jäggi, N. *et al.* Creation of Lunar and Hermean analogue mineral powder samples for solar wind irradiation experiments and mid-infrared spectra analysis. *Icarus* **365,** 114492 (2021).
70. Heiken, G. H., Vaniman, D. T. & French, B. M. *Lunar Sourcebook, a user's guide to the Moon* (1991).
71. McCoy, T. J., Peplowski, P. N., McCubbin, F. M. & Weider, S. Z. The geochemical and mineralogical diversity of Mercury. *Mercury. The View after MESSENGER. Edited by Sean C. Solomon,* 176–190 (2018).
72. Zolotov, M. Y. *et al.* The redox state, FeO content, and origin of sulfur-rich magmas on Mercury. *Journal of Geophysical Research: Planets* **118,** 138–146 (2013).
73. Eason, R. *Pulsed laser deposition of thin films: applications-led growth of functional materials* (John Wiley & Sons, 2007).
74. Fernandez-Pradas, J., Serra, P., Morenza, J. & De Aza, P. Pulsed laser deposition of pseudowollastonite coatings. *Biomaterials* **23,** 2057–2061 (2002).
75. Kuhlman, K. R., Sridharan, K. & Kvit, A. Simulation of solar wind space weathering in orthopyroxene. *Planetary and Space Science* **115,** 110–114 (2015).
76. Ramsier, R. & Yates Jr, J. Electron-stimulated desorption: Principles and applications. *Surface Science Reports* **12,** 246–378 (1991).
77. Voith, C. *Investigating the Angular Distribution of Sputtered Enstatite Atoms using a Catcher QCM Setup* Project Work. 2021.
78. Biber, H. *et al.* Solar wind Helium ion interaction with Mg and Fe rich pyroxene as Mercury surface analogue. *Nuclear Instruments and Methods in Physics Research Section B: Beam Interactions with Materials and Atoms* **480,** 10–15 (2020).

79. Szabo, P. *et al.* Experimental insights into space weathering of phobos: laboratory investigation of sputtering by atomic and molecular planetary ions. *Journal of Geophysical Research: Planets* **125,** e2020JE006583 (2020).

80. Gesell, D. *Erprobung eines Setups zur automatisierten Messung von Sputtering* Project Work. 2021.

81. Hofsäss, H. & Stegmaier, A. Binary collision approximation simulations of ion solid interaction without the concept of surface binding energies. *Nuclear Instruments and Methods in Physics Research Section B: Beam Interactions with Materials and Atoms* **517,** 49–62 (2022).

82. Carrez, P. *et al.* Low-energy helium ion irradiation-induced amorphization and chemical changes in olivine: Insights for silicate dust evolution in the interstellar medium. *Meteoritics & Planetary Science* **37,** 1599–1614 (2002).

83. Gault, D., Hörz, F., Brownlee, D. & Hartung, J. *Mixing of the lunar regolith* in *Lunar and planetary science conference proceedings* **5** (1974), 2365–2386.

84. Geiss, J., Bühler, F., Cerutti, H. & Eberhardta, P. 15. Solar-Wind Composition Experiment. *Apollo 15: Preliminary Science Report* **1** (1972).

Danksagung

Besonders in der Experimentalphysik ist das Gelingen eines Projekts selten das Wirken einer Einzelperson. So haben auch zu dieser Arbeit viele Leute beigetragen, bei denen ich mich an dieser Stelle bedanken möchte.

Zunächst danke ich dir, lieber Fritz. Du hast bereits in den Grundlagenvorlesungen im Bachelor einen bleibenden Eindruck hinterlassen, weswegen es mich sehr gefreut hat, als du mich per E-Mail gefragt hast, ob ich nicht auf eine Projektarbeit in deiner Gruppe vorbeischauen möchte. Dass dieser ersten PA eine zweite und auch schließlich diese Diplomarbeit gefolgt sind, ist unter anderem dem äußerst herzlichen Klima in deiner Arbeitsgruppe geschuldet, das du aktiv mitgestaltest. Danke für die exzellente Betreuung und auch die Förderung (und Forderung), die ich durch dich erfahren durfte. Ich freue mich bereits auf die Zusammenarbeit in den kommenden Jahren.

Auch dir, Herbert, gebührt mein Dank. Du schmeißt den Laden der BL3 äußerst souverän und ich bin jedes Mal aufs Neue von deinem weiten technischen Know-How erstaunt. Kein Problem könnte im Labor auftauchen, dem du nicht gewachsen wärst. Auch abseits der Physik konnte ich mein Allgemeinwissen in den Bereichen Film und Musik durch deine "Hausaufgaben" erweitern und es war stets eine Freude, mit dir über alles mögliche zu diskutieren. Ich hoffe, ich werde den Betrieb der BL3 so erfolgreich fortsetzen können, wie du ihn mir vorgelebt hast.

Weiters bedanke ich mich bei der gesamten Gruppe AG Atom- und Plasmaphysik, insbesondere den Mitgliedern des ~~Spaß~~Fusionsbüros. Martina, wir kollaborieren ja bereits seit dem ersten Semester äußerst erfolgreich. Bist a Maschin. Lidija, für das Buchführen unserer Dilemma und die Euphoniumkonzerte. Georg, für die kulinarische Betreuung. Redl, es freut mich sehr, dass bereits der dritte "Fan" in die Gruppe gefunden hat. Ich werde versuchen, dich in Zukunft beim Vornamen zu nennen. Natürlich darf auch der Rest der AG nicht unerwähnt bleiben: Anna, für das Lostreten der oben erwähnten Mail. Paul, für jegliche Unterstützung im Labor und sehr anregende abendliche und nächtliche Kaffeepausen. Christian, für Aufnahme und Einführung in die Fusion. Richard, für kulinarische Gespräche jeder Art und die Weitergabe deiner Expertise. Matthias, Helmut und Daniel für Frühstückspausen voller Kreuzworträtsel. Gabriel und David für alle Gespräche im Malina zu jeder Zeit.

Zu guter Letzt natürlich ein herzliches Danke meinen Eltern Eva und Gottfried. Ihr habt mich während meines ganzen Studiums stets bestärkt und unterstützt und in allen Lebenslagen beraten. Auch schwere Zeiten konnten wir gemeinsam durchstehen, wofür ich euch sehr dankbar bin. Ich bin froh, auch auf meinem weiteren Lebensweg auf eure Unterstützung bauen zu können.

Technical Drawings

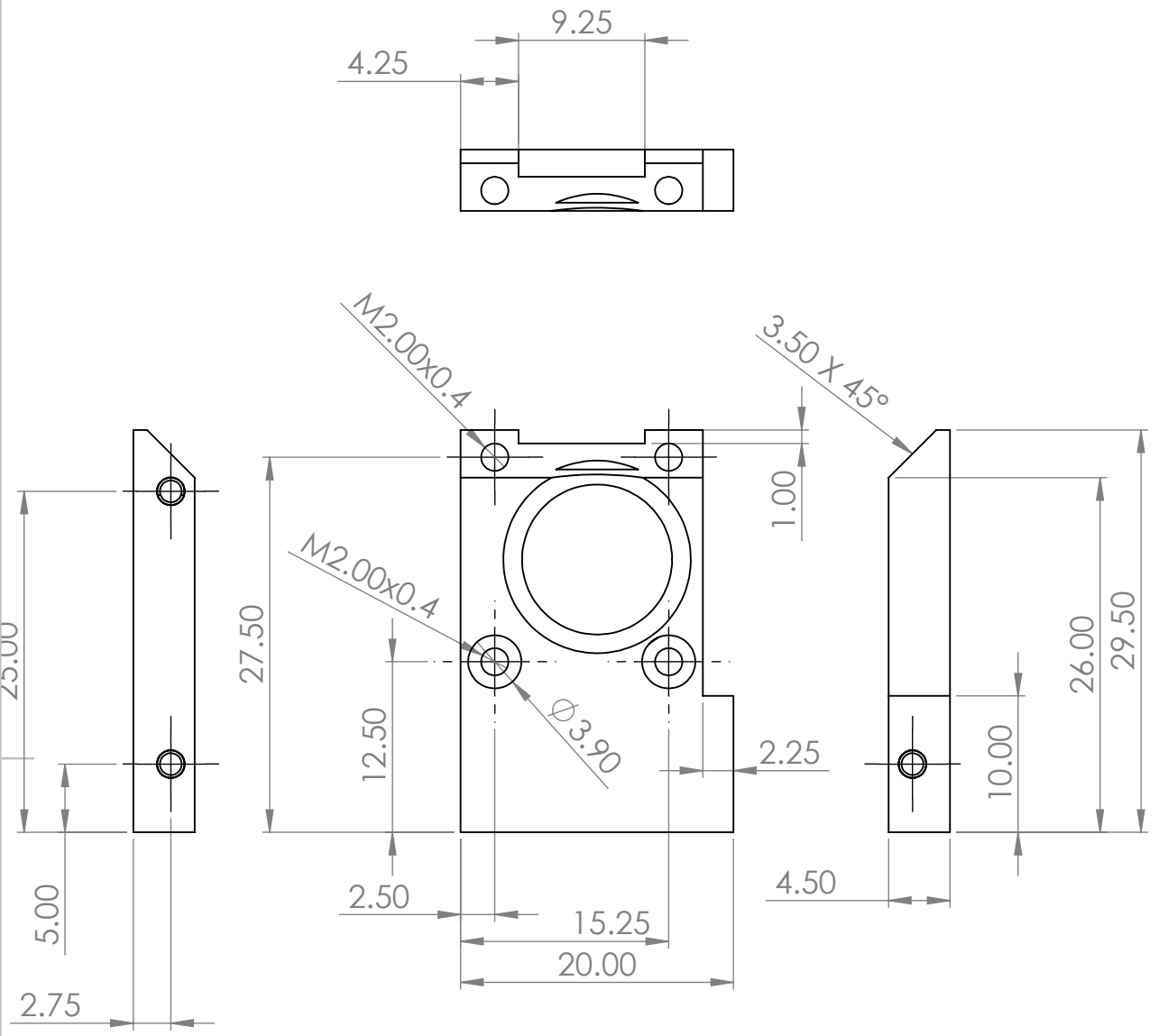

WENN NICHT ANDERS DEFINIERT: BEMASSUNGEN SIND IN MILLIMETER OBERFLÄCHENBESCHAFFENHEIT: TOLERANZEN: LINEAR: WINKEL:	OBERFLÄCHENGÜTE:	ENTGRATEN UND SCHARFE KANTEN BRECHEN	ZEICHNUNG NICHT SKALIEREN	ÄNDERUNG		
	NAME	SIGNATUR	DATUM			BENENNUNG:
GEZEICHNET						
GEPRÜFT						
GENEHMIGT						
PRODUKTION						
QUALITÄT				WERKSTOFF:	ZEICHNUNGSNR.	A4
					Catcher_Halter_neu	
				GEWICHT:	MASSSTAB:2:1	BLATT 1 VON 2

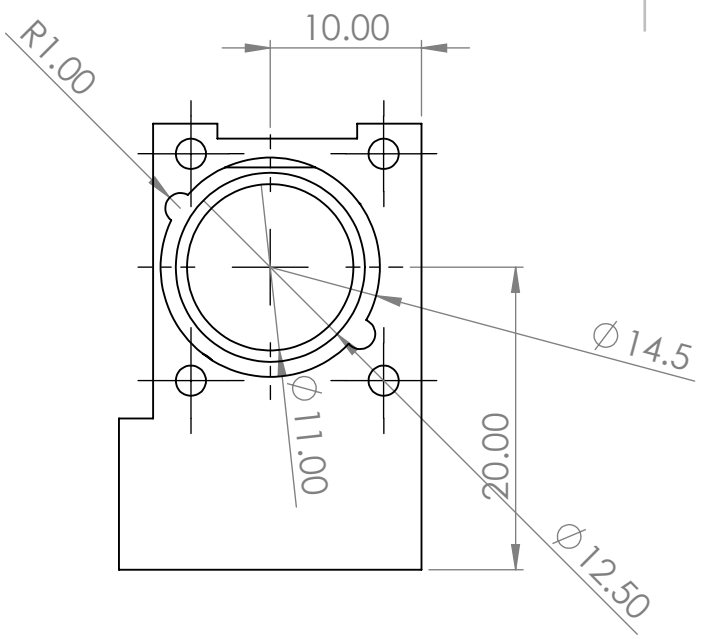

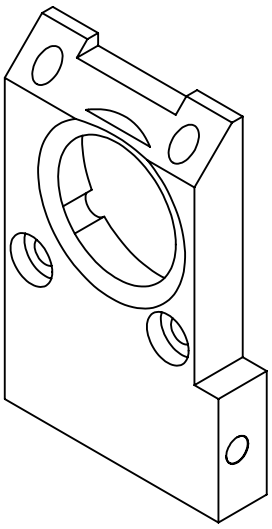

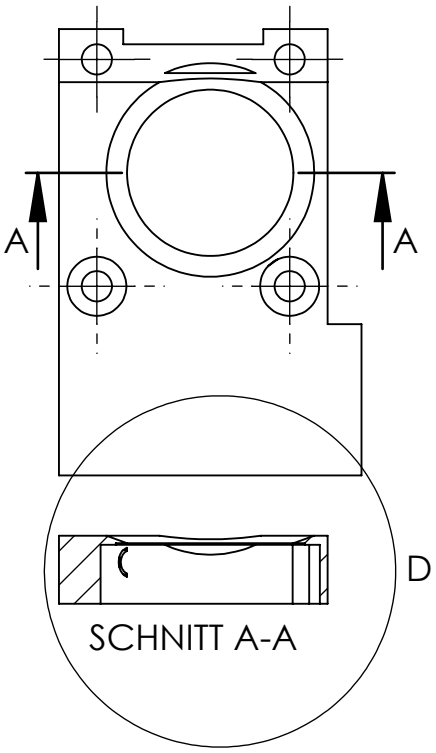

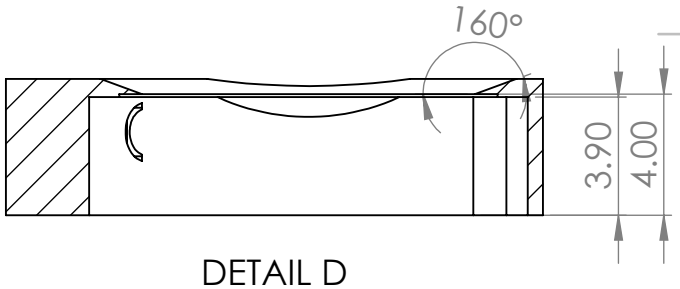

DETAIL D
MAßSTAB 4 : 1

WENN NICHT ANDERS DEFINIERT: BEMASSUNGEN SIND IN MILLIMETER OBERFLÄCHENBESCHAFFENHEIT: TOLERANZEN: LINEAR: WINKEL:	OBERFLÄCHENGÜTE:	ENTGRATEN UND SCHARFE KANTEN BRECHEN	ZEICHNUNG NICHT SKALIEREN	ÄNDERUNG		
	NAME	SIGNATUR	DATUM			BENENNUNG:
GEZEICHNET						
GEPRÜFT						
GENEHMIGT						
PRODUKTION						
QUALITÄT				WERKSTOFF:	ZEICHNUNGSNR.	A4
					Catcher_Halter_neu	
				GEWICHT:	MASSSTAB:2:1	BLATT 2 VON 2